Dept. of Biomedical Engineering and Computational Science

Method development for ultra-low-field magnetic resonance imaging and magnetoencephalography

Juhani Dabek

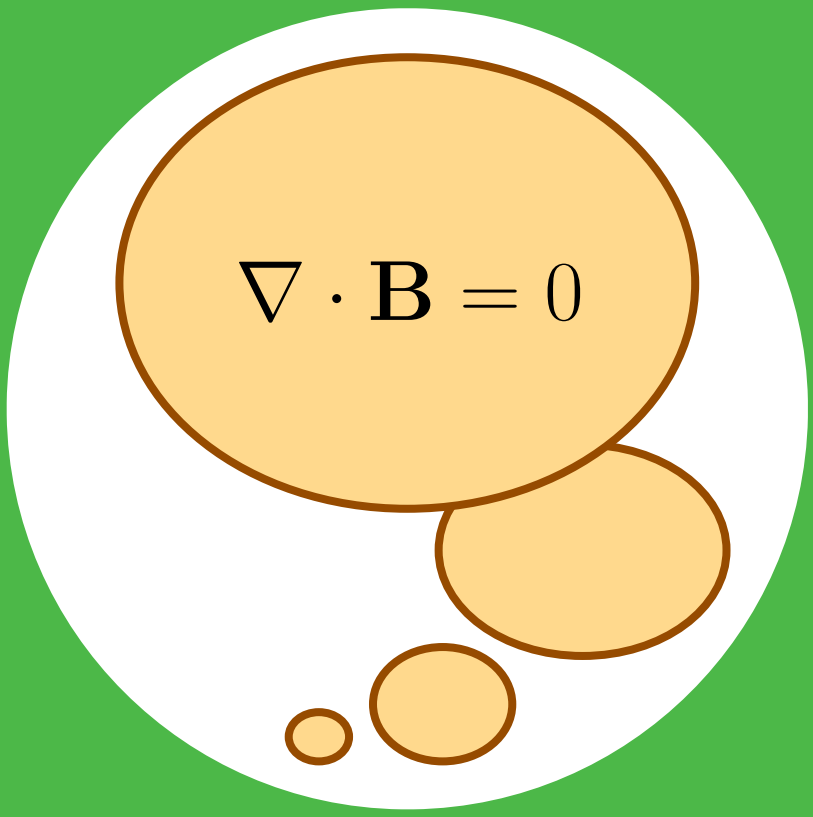

Aalto University

DOCTORAL DISSERTATIONS

Aalto University publication series
DOCTORAL DISSERTATIONS 42/2014

Method development for ultra-low-field magnetic resonance imaging and magnetoencephalography

Juhani Dabek

Doctoral dissertation for the degree of Doctor of Science in Technology (Doctor of Philosophy) to be presented with due permission of the School of Science for public examination and debate in Auditorium F239a at the Aalto University School of Science (Espoo, Finland) on the 29th of April 2014 at 12 noon.

Aalto University
School of Science
Dept. of Biomedical Engineering and Computational Science

Supervising professor
Prof. Risto Ilmoniemi

Thesis advisor
Prof. Risto Ilmoniemi

Preliminary examiners
Prof. Olli Gröhn, University of Eastern Finland, Finland
Dr. Michelle Espy, Los Alamos National Laboratory, USA

Opponent
Prof. Leif Østergaard, Aarhus University, Denmark

Aalto University publication series
DOCTORAL DISSERTATIONS 42/2014

ISBN 978-952-60-5629-6
ISBN 978-952-60-5630-2 (pdf)
ISSN-L 1799-4934
ISSN 1799-4934 (printed)
ISSN 1799-4942 (pdf)
http://urn.fi/URN:ISBN:978-952-60-5630-2

Unigrafia Oy
Helsinki 2014

Finland

441 697
Printed matter

Author
Juhani Dabek

Name of the doctoral dissertation
Method development for ultra-low-field magnetic resonance imaging and magnetoencephalography

Publisher School of Science

Unit Department of Biomedical Engineering and Computational Science

Series Aalto University publication series DOCTORAL DISSERTATIONS 42/2014

Field of research Biomedical Engineering

Manuscript submitted 11 February 2014 **Date of the defence** 29 April 2014

Permission to publish granted (date) 2 April 2014 **Language** English

☐ **Monograph** ☒ **Article dissertation (summary + original articles)**

Abstract

Ultra-low-field (ULF) magnetic resonance imaging (MRI) can be combined with magnetoencephalography (MEG) in a hybrid MEG-MRI device using superconducting quantum interference device (SQUID) sensors for measuring both MRI (structural imaging) and MEG (functional imaging) signals. The MEG-MRI device, which has an open structure, is situated in a magnetically shielded room to suppress magnetic field noise. The ULF-MRI device can be operated with relaxed safety considerations compared to conventional MRI because of the absence of very strong magnetic fields. MEG has grown into an important multichannel neuroimaging modality in the past 20 years with research and clinical applications. Low-field (LF) MRI, with field strength between that of ULF and conventional MRI, cannot accommodate MEG today but may grow in importance with the development of giant-magnetoresistive (GMR) mixed sensors.

In this dissertation, methods for MRI and MEG have been developed, with an emphasis on ultra-low- and low-field applications. The necessary physical and signal-processing basis is reviewed, accompanied by new methodological improvements. The safety of low magnetic fields is investigated, modelling of the free induction decay (FID) signal underlying MRI is improved and the developed gradient-excitation-encoding method is tested by simulation. A new quantitative method for ULF-MRI device calibration and determination of, for example, sample water content is developed and validated. GMR mixed sensors are applied in LF MRI, resulting in a high signal-to-noise ratio and contrast-to-noise ratio. Eventually, a new method for power correlations between brainwaves is developed and tested on MEG data. The presented methods aim at improvements in the use of the two imaging modalities.

Keywords Brain imaging, magnetic resonance imaging, MRI, ultra-low-field MRI, low-field MRI, magnetoencephalography, MEG, SQUID, GMR, mixed sensor

ISBN (printed) 978-952-60-5629-6 **ISBN (pdf)** 978-952-60-5630-2

ISSN-L 1799-4934 **ISSN (printed)** 1799-4934 **ISSN (pdf)** 1799-4942

Location of publisher Helsinki **Location of printing** Helsinki **Year** 2014

Pages 150 **urn** http://urn.fi/URN:ISBN:978-952-60-5630-2

Aalto-yliopisto

Tiivistelmä

Aalto-yliopisto, PL 11000, 00076 Aalto www.aalto.fi

Tekijä
Juhani Dabek

Väitöskirjan nimi
Menetelmäkehitystä ultramatalien kenttien magneettikuvaukseen ja magnetoenkefalografiaan

Julkaisija Perustieteiden korkeakoulu

Yksikkö Lääketieteellisen tekniikan ja laskennallisen tieteen laitos

Sarja Aalto University publication series DOCTORAL DISSERTATIONS 42/2014

Tutkimusala Lääketieteellinen tekniikka

Käsikirjoituksen pvm 11.02.2014 **Väitöspäivä** 29.04.2014

Julkaisuluvan myöntämispäivä 02.04.2014 **Kieli** Englanti

☐ **Monografia** ☒ **Yhdistelmäväitöskirja (yhteenveto-osa + erillisartikkelit)**

Tiivistelmä

Ultramatalien kenttien magneettikuvaus (ultra-low-field magnetic resonance imaging, ULF-MRI) ja magnetoenkefalografia (MEG) voidaan yhdistää MEG–MRI-laitteessa käyttäen ultraherkkiä magneettikenttäantureita (superconducting quantum interference device eli SQUID-antureita), jotka mittaavat sekä MRI- (rakenteellinen kuvantaminen) että MEG-signaalit (funktionaalinen kuvantaminen). Avararakenteinen MEG–MRI-laite sijoitetaan magneettikenttähäiriöiden vaimentamiseksi magneettisesti suojattuun huoneeseen. Koska voimakkaita magneettikenttiä ei käytetä ULF-MRI-laitteessa, huomioon otettavia turvallisuusnäkökohtia on vähemmän. Monikanavainen MEG on kasvanut viimeisen 20 vuoden aikana tärkeäksi aivokuvantamismenetelmäksi, jolla on sovelluksia sekä tutkimuksessa että kliinisesti. MEG:tä ei toistaiseksi voida yhdistää matalan kentän (low-field, LF) MRI:hin, jossa kentänvoimakkuus on ULF-MRI:n ja tavanomaisen MRI:n väliltä, mutta LF-MRI:n merkitys saattaa kasvaa suureen magnetoresistanssiin (giant magnetoresistance, GMR) perustuvien anturien (GMR mixed sensor) kehittyessä.

Tässä väitöskirjatyössä on kehitetty menetelmiä MRI:hin ja MEG:hen, painottaen ultramatalan ja matalan kentän sovelluksia. Uusiin menetelmällisiin parannuksiin tutustutaan tarvittavan fysikaalisen perustan ja signaalinkäsittelyn myötä. Työssä on tutkittu matalien magneettikenttien turvallisuutta, parannettu MRI:n perustana olevan vaimenevan sinisignaalin (free induction decay, FID) mallinnusta ja simuloitu uutta kehitettyä gradienttivirityskoodausmenetelmää (gradient-excitation encoding). ULF-MRI-laitteen kalibrointiin ja esimerkiksi näytteen vesimäärän arviointiin on kehitetty uusi kvantitatiivinen menetelmä, jonka toiminta varmistettiin mittauksin. LF-MRI:ssä on sovellettu GMR-antureita, joilla saatiin kuvia voimakkaalla signaalilla ja vahvalla kontrastilla suhteessa kohinaan. Aivoaaltojen välisten tehokorrelaatioiden arviointiin on kehitetty uusi menetelmä ja sitä testattiin MEG-mittauksin. Esitetyt menetelmät tähtäävät parannuksiin MRI- ja MEG-kuvantamismenetelmien käytössä.

Avainsanat Aivokuvantaminen, magneettikuvaus, MRI, ultramatalien kenttien MRI, matalien kenttien MRI, magnetoenkefalografia, MEG, SQUID-anturi, GMR-anturi

ISBN (painettu) 978-952-60-5629-6 **ISBN (pdf)** 978-952-60-5630-2

ISSN-L 1799-4934 **ISSN (painettu)** 1799-4934 **ISSN (pdf)** 1799-4942

Julkaisupaikka Helsinki **Painopaikka** Helsinki **Vuosi** 2014

Sivumäärä 150 **urn** http://urn.fi/URN:ISBN:978-952-60-5630-2

Aalto-universitetet

Sammandrag

Aalto-universitetet, PB 11000, 00076 Aalto www.aalto.fi

Författare
Juhani Dabek

Doktorsavhandlingens titel
Metodutveckling för ultralågfälts magnetisk resonansavbildning och magnetoenkefalografi

Utgivare Högskolan för teknikvetenskaper

Enhet Institutionen för medicinsk teknik och beräkningsvetenskap

Seriens namn Aalto University publication series DOCTORAL DISSERTATIONS 42/2014

Forskningsområde Medicinsk teknik

Inlämningsdatum för manuskript 11.02.2014 **Datum för disputation** 29.04.2014

Beviljande av publiceringstillstånd (datum) 02.04.2014 **Språk** Engelska

☐ **Monografi** ☒ **Sammanläggningsavhandling (sammandrag plus separata artiklar)**

Sammandrag

Ultralågfälts (ULF) magnetisk resonansavbildning (magnetic resonance imaging, MRI) kan kombineras med magnetoenkefalografi (MEG) i en apparat med ultrakänsliga magnetfältdetektorer (superconducting quantum interference device dvs. SQUID-detektorer) för mätning av både MRI- (strukturell avbildning) och MEG-signaler (funktionell avbildning). MEG–MRI-apparaten, som har en öppen struktur, är installerad i ett magnetiskt skyddsrum för att dämpa magnetiskt fältbrus. På grund av bristen på höga magnetfält är trygghetskraven lindrigare i ULF-MRI än i konventionell MRI. MEG har utvecklats till en viktig hjärnavbildningsmetod under de senaste 20 åren med tillämpningar i forskning och klinik. Lågfälts (LF) MRI, med fältstyrka mellan den av ULF-MRI och konventionell MRI, kan inte för närvarande kombineras med MEG men dess betydelse torde öka med utvecklingen av detektorer med jättemagnetoresistans (giant magnetoresistance, GMR, mixed sensors).

I den här doktorsavhandlingen har metoder för MRI och MEG utvecklats, med betoning på ULF- och LF-tillämpningar. Det nödvändiga underlaget i fysik och signalbehandling genomgås med nya metodologiska framsteg. Tryggheten av låga magnetfält har undersökts, beskrivningen av den dämpande sinusvågen (free induction decay, FID), som är grundläggande i MRI, har förbättrats och den utvecklade gradientexciteringskodningsmetoden har simulerats. En ny kvantitativ metod för kalibreringen av ULF-MRI-apparaten och bestämmandet av till exempel vatteninnehållet av ett prov har utvecklats och kontrollerats med uppmätningar. GMR-detektorer har tillämpats på LF-MRI med hög signalbrus- och kontrastbrusförhållande. Till sist har kopplingen mellan hjärnvågor uppskattats med hjälp av effektkorrelationer och utvärderats med MEG-data. De introducerade metoderna siktar mot förbättringar i tillämpningar av de två avbildningsmetoderna.

Nyckelord Hjärnavbildning, magnetisk resonansavbildning, MRI, ultralågfälts MRI, lågfälts MRI, magnetoenkefalografi, MEG, SQUID-detektor, GMR-detektor

ISBN (tryckt) 978-952-60-5629-6	**ISBN (pdf)** 978-952-60-5630-2	
ISSN-L 1799-4934	**ISSN (tryckt)** 1799-4934	**ISSN (pdf)** 1799-4942
Utgivningsort Helsingfors	**Tryckort** Helsingfors	**År** 2014
Sidantal 150	**urn** http://urn.fi/URN:ISBN:978-952-60-5630-2	

Preface and Acknowledgements

Professor Risto Ilmoniemi in 2007 introduced me to the fascinating and important field which forms the substance of this Thesis. I am indebted to him not only for this, but also for the firm and kind support he has given me over the years. I am also grateful for the encouraging atmosphere in my workplace, the Department of Biomedical Engineering and Computational Science (BECS) at Aalto University School of Science. Looking back at my early career in the Laboratory of Biomedical Engineering (BME) of Helsinki University of Technology (TKK), I am also indebted to Prof. emer. Toivo Katila for an inspiring working environment, as well as Juha Montonen and Jukka Nenonen for the summer employee interview in 2001 after which they recruited me as a research assistant in the cardiac research group. Until 2007, Heikki Väänänen was my instructor and guided me in signal analysis programming with expertise. Over the years, I have been privileged to conduct my undergraduate studies parallelling cardiac research and postgraduate studies concerning combined ultra-low-field (ULF) magnetic resonance imaging (MRI) and magnetoencephalography (MEG) in BME and BECS, close to the research fields lead by Profs. Ari Koskelainen (biophysics), Pekka Meriläinen (jointly between BME and GE Medical), Jukka Sarvas (mathematical modelling), Lauri Parkkonen (MEG), and also Prof. Raimo Sepponen of the Department of Electrical Engineering and Automation as well as Prof. Fa-Hsuan Lin from Taiwan. Prof. Sepponen has inspired me with subjects related to MRI, helping me in the process of compiling three of my dissertation publications. Naturally, I also wish to thank Prof. Jouko Lampinen for heading BECS in a productive way resulting in an excellent working atmosphere.

My PhD work has been supported by a few select organisations over the years. Regarding my research in MEG-MRI, I acknowledge the funding from the European Community's Seventh Framework Programme (FP/2007-2013) under Grant Agreement No. 200859, as well as the Finnish Foundation for Technology Promotion (TES), the Väisälä Foundation and the International Doctoral Programme in Biomedical Engineering and Medical Physics (iBioMEP).

Following the years in cardiac research my transition to MEG-MRI was diversified from 2006 to 2008 by participation in the Helsinki School of Creative Entrepreneurship (HSCE) initiated by Peter Kelly. I saw it as my first step towards working at Aalto University while promoting the heart monitor project (proposed by Heikki Väänänen) on behalf of TKK among students from TKK, Helsinki School of Economics (HSE) and University of Art and Design Helsinki (TaiK). TKK, HSE and TaiK merged into Aalto University in 2010.

In my postgraduate studies under the supervision and instruction of Prof. Ilmoniemi, I started to familiarize myself with ULF MRI together with Jaakko Nieminen and Panu Vesanen. Both of them showed admirable skills in physics and determination in doing their M.Sc. (Tech.) and D.Sc. (Tech.) qualifications. Later, Koos Zevenhoven, with matching skills and determination, joined the group in the phase of designing our MEG-MRI device (MEGMRI project, FP/2007-2013). Over the years, Mika Pollari, Fredrik Sannholm, Reko Kemppainen, Sarianna Alanko, Juho Luomahaara, Andrey Zhdanov, Nadia Catallo and Yi-Cheng Hsu have promoted the MEGMRI project; its success depended also largely on the contributions by Jyrki Mäkelä, Antti Ahonen, Juha Simola, Juha Hassel and Jari Penttilä. On the international front I thank Prof. Claude Fermon for the fine opportunity in 2010 of working four months in Saclay, France during the MEGMRI project, and I am grateful to Natalia Sergeeva-Chollet who instructed me there in developing giant-magnetoresistive (GMR) mixed sensors and operating the low-field (LF) MRI device; I also extend my gratitude to Myriam Pannetier-Lecoeur, Hadrien Dyvorne, Hedwige Polovy and Remy Lassalle-Balier. Regarding my last PhD Publication, I am indebted to Vadim Nikulin for his important contributions. At BECS, I have shared many great moments with my colleagues, especially with Teijo Konttila, Ville Mäntynen, Matti Stenroos, Julio Hernández Pavón and Ilkka Nissilä over so many years up to the present day. Regarding my Thesis directly, I am particularly thankful to Dr. Michelle Espy and Prof. Olli Gröhn for their expertise and the thorough work they bestowed on the pre-examination.

I address my final thanks to my father, mother and brother with his family. Their love and support over the years have been the foundation of my life. Today, my lovely wife Kaisa belongs to the same foundation. She has witnessed my everyday struggle and success towards the dissertation and I am grateful for her loving support.

Helsinki, Friday 4th April 2014,

Juhani Dabek

Contents

List of Publications

This Thesis consists of an overview and of the following Publications which are referred to in the text by their Roman numerals.

I J. Dabek, F. Sannholm, J. O. Nieminen, P. T. Vesanen and R. J. Ilmoniemi. Safety in simultaneous ultra-low-field MRI and MEG: Forces exerted on magnetizable objects by magnetic fields. In *IFMBE Proceedings*, 28: 74–77, Biomag 2010 Conference, Dubrovnik, Croatia, 2010.

II J. Dabek, J. O. Nieminen, P. T. Vesanen, R. Sepponen and R. J. Ilmoniemi. Improved determination of FID signal parameters in low-field MRI. *Journal of Magnetic Resonance*, 205: 148–160, 2010.

III N. Sergeeva-Chollet, H. Dyvorne, J. Dabek, Q. Herreros, H. Polovy, G. Le Goff, G. Cannies, M. Pannetier-Lecoeur and C. Fermon. Low field MRI with magnetoresistive mixed sensors. In *Journal of Physics: Conference Series*, 303: 012055, JEMS 2010 Conference, Krakow, Poland, 2011.

IV J. Dabek, K. C. J. Zevenhoven, J. O. Nieminen, P. T. Vesanen, R. Sepponen and R. J. Ilmoniemi. Gradient-excitation encoding combined with frequency and phase encodings for three-dimensional ultra-low-field MRI. In *IEEE EMBS Proceedings*, 1093–1097, EMBC 2012 Conference, San Diego, CA, USA, 2012.

V J. Dabek, P. T. Vesanen, K. C. J. Zevenhoven, J. O. Nieminen, R. Sepponen and R. J. Ilmoniemi. SQUID-sensor-based ultra-low-field MRI calibration with phantom images: Towards quantitative imaging. *Journal of Magnetic Resonance*, 224: 22–31, 2012.

VI J. Dabek, V. V. Nikulin and R. J. Ilmoniemi. Detecting millisecond-range coupling delays between brainwaves in terms of power correlations by magnetoencephalography. Submitted to *Journal of Neuroscience Methods*, 16 pages, 2014.

Author's Contribution

Publication I: "Safety in simultaneous ultra-low-field MRI and MEG: Forces exerted on magnetizable objects by magnetic fields"

The author was responsible for planning the measurements and had a main role in carrying them out. The author was the main developer of the theory and he carried out the simulations and data analysis. He is the principal author of the publication.

Publication II: "Improved determination of FID signal parameters in low-field MRI"

The author participated in designing and carrying out the measurements. He invented the theory and was the main person developing it. He performed the simulations and analysed the results. He is the principal author of the article.

Publication III: "Low field MRI with magnetoresistive mixed sensors"

The author participated in the work related to sensor development as well as in testing the imaging system. He took part in revising the manuscript.

Publication IV: "Gradient-excitation encoding combined with frequency and phase encodings for three-dimensional ultra-low-field MRI"

The author was the inventor and main developer of the method with related simulations and analysis. He is the principal author of the publication.

Publication V: "SQUID-sensor-based ultra-low-field MRI calibration with phantom images: Towards quantitative imaging"

The author took part in constructing the measurement system. He created the theoretical framework and analysed the measurements accordingly. He is the principal author of the article.

Publication VI: "Detecting millisecond-range coupling delays between brainwaves in terms of power correlations by magnetoencephalography"

The author performed the measurements of two out of three subjects, invented the theoretical framework and analysed the data. He is the principal author of the article.

List of Figures

List of Tables

Nomenclature

α	Flip angle
α_1	T_1 relaxivity of a CA
α_{Ernst}	Ernst angle
$\lvert\mathbf{m}\rvert$	Magnetic moment amplitude
$\boldsymbol{\beta}(\mathbf{r})$	Coil lead field, or, sensitivity to magnetic moment
χ	Magnetic susceptibility
Δ	Change
δ	Small change
δ_R	Resistance change per magnetic field change
$\Delta x \times \Delta y \times \Delta z$	Voxel dimensions
$\eta(t)$	Noise in FID measurement
$\exp(i\varphi)$	Complex phase factor, $e^{i\varphi}$
γ	Proton gyromagnetic ratio, $2\pi \cdot 42.58$ MHz/T
γ_{H}	Hooge constant
$\hat{\mathbf{e}}_x$	Unit vector in the x direction
$\hat{\mathbf{e}}_y$	Unit vector in the y direction
$\hat{\mathbf{e}}_z$	Unit vector in the z direction
$\hat{\omega}_1$	B_1 tilting angular frequency
$\hat{I}$	Desired signal amplitude
$\lfloor\cdot\rfloor$	Rounding down
$\mathbf{B}$	Magnetic field
$\mathbf{E}$	Electric field
$\mathbf{F}$	Force (gravity)
$\mathbf{H}_{\text{h}}$	Hard layer magnetizing field
$\mathbf{H}_{\text{s}}$	Soft layer magnetizing field
$\mathbf{J}$	Current density
$\mathbf{L}$	Angular momentum
$\mathbf{M}$	Magnetization

$\mathbf{M}'(t)$	Magnetization in rotating frame of reference
$\mathbf{M}_{xy}$	Transverse component of magnetization
$\mathbf{r}$	Position
$\mathbf{S}$	Spin angular moment vector
$\mathbf{v}$	Velocity
$\mathcal{R}$	Two-dimensional Radon transform
$\mathrm{Im}\{s(t)\}$	Quadrature-detected imaginary (Im) part of $s(t)$
$\mathrm{Re}\{s(t)\}$	Measured (real, Re) part of $s(t)$
μ	Spin magnetic moment
μ_0	Vacuum permeability
μ_r	Relative permeability
$\mu\mathrm{T}$	microtesla, 10^{-6} T
ν_s	Sampling frequency
ν_max	Signal maximum frequency
Ω	Frequency variable
ω_0	Angular Larmor frequency, $2\pi f_0$
$\Phi(t)$	Flux through coil over time
Φ_0	Flux quantum, $h/2e$
Φ_a	Applied magnetic flux
$\pm\tilde{\mathbf{H}}$	Magnetizing field
ρ	Charge density
ρ_s	Spin density
σ_n	Standard deviation of background noise
$\mathrm{sinc}\, x$	sinc function, $\sim \sin x/x$
τ	Duration
τ_c	Correlation time
Θ	Absolute temperature
θ_m	Magic angle, $\sim 54.7°$
ε_0	Vacuum permittivity
φ	Signal phase
$\widehat{f}(\omega)$	Fourier transform of f
ξ	One-dimensional imaging location
$^1\mathrm{H}$	Hydrogen isotope without neutrons
$^\circ\mathrm{C}$	Degree Celsius
A	FID amplitude
B_0	Measurement field
B_1	RF field to nutate magnetization
B_p	Prepolarization field

C	Capacitance
e	Elementary charge, $1.602 \cdot 10^{-19}$ C
E_{s_z}	Proton spin splitting energy
f	Frequency
f_0	Larmor frequency, $\omega_0/2\pi$
G	Flux-transformer gain
G_s	Slice-selection gradient
G_ω	Frequency-encoding gradient
G_x, G_y and G_z	x, y and z gradients
G_1	Dephasing gradient allowing refocusing
G_2	Dephasing gradient resisting refocusing
$G_{y,p'}$ and $G_{z,q'}$	Stepped y and z gradients
I	Electric current
i	Imaginary unit, $i^2 = -1$
I_A and I_B	Pixel grayscale values for tissues A and B
I_b	Bias current
I_c	Critical current
I_n	Voxel intensity
k-space	Space of spatial frequencies
k_B	Boltzmann constant, $1.38 \cdot 10^{-23}$ J/K
L	Inductance
$L_x \times L_y \times L_z$	FOV volume
$M(x)$	Magnetization at x
$M_{z,\infty}$	Equilibrium magnetization in z direction
$N \times P \times Q$	Voxel count of a three-dimensional sample
N_c	Number of charge carriers
$N_\uparrow + N_\downarrow$	Sum of number of protons with spin up and down
$N_x \times N_y \times N_z$	Three-dimensional voxel count
$n_{V,1/f}$	$1/f$-noise
$n_{V,\mathrm{therm}}$	Thermal noise
p	Position on a projection line in backprojection imaging
q_c	Charge
R	Resistance
R_acc	Acceleration factor
$R_\uparrow$ and $R_\downarrow$	Spin-up and spin-down resistances
S	Spin angular moment
s	Principal quantum number
s_z	Projection quantum number along z axis

t	Time
T_1	Longitudinal relaxation time
T_2	Transverse relaxation time
T_2^*	Relaxation time affected by field inhomogeneity ($T_2^* < T_2$)
T_2^{**}	Short relaxation time in GE ($T_2^{**} < T_2^*$)
T_c	Critical temperature
T_E	Echo time
T_R	Repetition interval
$T_{1,\mathrm{eff}}$	Effective T_1
$T_{1,A},\ T_{1,B}$	T_1 for tissues A and B
$u(t)$	Induced voltage
V	Voltage
x	First Cartesian coordinate
y	Second Cartesian coordinate
z	Third Cartesian coordinate
2D	Two-dimensional
A	ampere
a.u.	Arbitrary unit
Al	Aluminium
BOLD	Blood-oxygen-level dependent (fMRI contrast)
BSS	Blind source separation
C	coulomb
CA	Contrast agent
CDI	Current density imaging
cm	centimetre, 10^{-2} m
CNR	Contrast-to-noise ratio
CSF	Cerebospinal fluid
CT	Computed tomography
dB	decibel
DC	Direct current
dHb	Deoxyhaemoglobin
DNI	Direct neural imaging
DNP	Dynamic nuclear polarization
ECD	Equivalent current dipole
EEG	Electroencephalography
EPI	Echo-planar imaging
FFT	Fast Fourier transform
FID	Free induction decay

fMRI	Functional MRI
FOV	field of view
FOV_y and FOV_z	FOVs in y and z directions
fT	femtotesla, 10^{-15} T
gauss	0.1 mT
GE	Gradient-echo
GEE	Gradient-excitation encoding
GMR	Giant magnetoresistance
GRAPPA	Generalized autocalibrating partially parallel acquisitions
H_2O	Water, hydrogen oxide
Hb	Oxyhaemoglobin
He	Helium
HFO	High-frequency oscillation
Hz	hertz, 1/s
ICA	Independent component analysis
Js	joule-second
K	kelvin
kg	kilogram
kHz	kilohertz, 10^3 Hz
LF MRI	Low-field MRI
MCG	Magnetocardiography
MEG	Magnetoencephalography
min	minute
mm	millimetre, 10^{-3} m (metre)
MMN	Mismatch negativity
MNE	Minimum norm estimate
MRI	Magnetic resonance imaging
ms	millisecond, 10^{-3} s
MSR	Magnetically shielded room
mT	millitesla
MUSIC	Multiple signal classification
mV	millivolt, 10^{-3} V
N_2	Nitrogen (molecular)
Nb	Niobium
$NiCl_2$	Nickel chloride
NIRS	Near-infrared spectroscopy
NMR	Nuclear magnetic resonance
Pb	Lead (plumbum)

PC	Power correlation
PCA	Principal components analysis
PET	Positron emission tomography
PILS	Partially parallel imaging with localized sensitivities
PNS	Peripheral nerve stimulation
ppm	parts per million
PSF	Point-spread function
RF	Radio frequency
s	second
SAR	Specific absorption rate
SE	Spin echo
SENSE	Sensitivity encoding
SMASH	Simultaneous acquisition of spatial harmonics
SNR	Signal-to-noise ratio
SPECT	Single-photon emission computed tomography
SQUID	Superconducting quantum interference device
SSD	Spatio-spectral decomposition
SSP	Signal-space projection
SSS	Signal-space separation
SVD	Singular value decomposition
T	tesla
THK	Slice thickness
Ti	Titanium
TMS	Transcranial magnetic stimulation
ton	1000 kg
TSE	Turbo spin echo
Tx and Rx	Transmission and detection (coils)
ULF MRI	Ultra-low-field MRI
US	Ultrasound
V	volt
VEF	Visual evoked field
Wb	weber
YBCO	Yttrium barium copper oxide, $YBa_2Cu_3O_{7-x}$

1. Introduction

The human brain has circa 10^{11} neurons and 10^{14} synapses that allow the communication between the neurons. The structure of the living brain can be imaged non-invasively with magnetic resonance imaging (MRI), whereas computed tomography (CT, volumetric imaging with X-rays) involves ionizing radiation. The function of the brain can be studied non-invasively with magnetoencephalography (MEG) by observing the weak magnetic fields originating mainly from the cortical synaptic signalling. In addition, functional MRI (fMRI), electroencephalography (EEG, measurement with electrodes placed on scalp) and near-infrared spectroscopy (NIRS, probing the brain with infrared light) allow non-invasive studies of brain activity, but positron emission tomography (PET, detection of gamma-ray pairs) and single-photon emission computed tomography (SPECT, detection of single gamma rays) apply ionizing radiation. Furthermore, transcranial magnetic stimulation (TMS, local brain activation elicited by pulsed magnetic field) can be used to map brain functionality. The work in this Thesis concentrates on MRI in low and ultra-low fields (LF MRI and ULF MRI) and MEG.

The voxel size in conventional MRI can be 1 mm^3, so in a brain volume of 10^6 mm^3, there are one million voxels. Thus, each voxel could contain on average 10^5 neurons and 10^8 synapses. On the other hand, it has been estimated that at least some 10^4 neurons should be simultaneously active in the cortex for feasible MEG detection. These estimates show that both MRI and MEG investigate structure and function that are clearly coarse-grained. However, these technologies that were introduced in the late 20^{th} century are very powerful and can help in understanding the human brain and its function. In the following sections, the history and background relating to the research field is briefly introduced.

1.1 Research field

MRI is an application of nuclear magnetic resonance (NMR) which was initially discovered in hydrogen beams by I.I. Rabi (Nobel Prize 1944). Later, F. Bloch and E.M. Purcell extended NMR into solids and liquids (Nobel 1952). The first MRI device was developed by R.V. Damadian [Damadian, 1972], but the preceding work of P.C. Lauterbur and P. Mansfield with the use of gradient fields in the 1970s is considered as the basis of modern MRI. The two latter were awarded the Nobel prize in 2003 *for their discoveries concerning magnetic resonance imaging*, although there is dispute whether Damadian should also have been one of the laureates. The development of MRI can be summed up in fundamental discoveries of physics:

- Lorentz and Zeeman (Nobel 1902)
  Anomalous Zeeman effect (1896): electron spin.
- Stern (Nobel 1943) and Gerlach
  Stern-Gerlach experiment (1920): nuclear spin.
- Rabi (Nobel 1944)
  Rabi's experiment (1937): NMR.
- Bloch and Purcell (Nobel 1952)
  NMR for solids and liquids, containing ^{1}H.
- Lauterbur and Mansfield (Nobel 2003), and Damadian
  MRI (Damadian's patent 1972).
- Today: big manufacturers of MRI devices
  GE, Siemens, Philips, Hitachi, Toshiba, FONAR, Varian, Bruker, ...

Today, there are thousands of MRI scanners around the world in clinical use. They commonly have a field strength of 1.5 or 3 T, and scanners with even higher fields are developed (experimentally highest ones 9.4 T for humans and 21.1 T for animals), to enhance the signal-to-noise ratio (SNR) and resolution. In the USA, on the average 1 MRI experiment per 10 people was performed in 2011 with other countries trailing [OECD, 2013]. The importance of MRI as a clinical tool is so high that regardless of the high assembly and running costs (construction of the device with a superconducting coil, cooling with liquid helium, safety precautions because of the strong magnetic fields, highly educated personnel *etc.*), the market keeps growing. MRI is best suited for the study of soft tissue, and thus brain MRI is particularly useful. With appropriate imaging sequences, various tissues can be emphasized and fMRI can map brain activity with 1-s resolution.

MEG was first measured by D. Cohen in 1968 with a million-turn coil [Cohen, 1968]. The detection of alpha waves that was achieved within a magnetically shielded room (MSR [Cohen, 1970]) was confirmed by comparison to a simultaneous EEG measurement. The real breakthrough of MEG began when the superconducting quantum interference device (SQUID [Silver and Zimmerman, 1965]) was adopted as the sensor [Cohen, 1972]. The first MEG system with 122 sensors covering the whole scalp area was completed in 1992 [Ahonen et al., 1993]. Since 1998, the modern state-of-the-art devices have 306 channels at 102 locations (Elekta Oy, Helsinki, Finland). MEG is an invaluable brain research tool, and clinically it is used mainly in preoperative mapping of the eloquent cortex and characterisation of epileptic activity. Currently, there are approximately one hundred 306-channel MEG devices around the world built by the market leader (Elekta Oy).

1.2 Research environment and phases of Thesis work

The background for this doctoral Thesis is best described by the research questions that arose during the four-year EU project (May 2008–April 2012) called MEGMRI that was coordinated by Aalto University (and its predecessor Helsinki University of Technology until the end of 2009) in Otaniemi. The intention of the project was to build a functional device for both MEG and ULF-MRI measurements. The cutting-edge research in ULF MRI was initiated to a large extent by the group of John Clarke in Berkeley [Clarke et al., 2007, Inglis et al., 2013], and significant development in MEG-MRI has originally come from Los Alamos [Zotev et al., 2007a, Magnelind et al., 2011].

The MEGMRI project in Otaniemi resulted in a fully functional MEG-MRI prototype [Vesanen et al., 2013a]. There was a project based in Otaniemi preceding MEGMRI, SQUID MRI, where the NMR signals underlying MRI were investigated with the SQUIDs of the magnetocardiography (MCG) device in the BioMag Laboratory (Helsinki University Central Hospital). The NMR free induction decay (FID) signal was obtained from water samples with prepolarization by an electromagnet as well as a strong permanent magnet.

The initial phase of the MEGMRI project started when the Department of Biomedical Engineering and Computational Science (BECS) had the division relevant to this Thesis, Biomedical Engineering, in temporary premises in Otaniemi, and part of the experiments were carried out at the premises of Elekta Oy in Helsinki. Publications I and II were composed primarily at that time. At the end of 2009, BECS finally came together and moved to the renovated old house of engineering physics. As planned, the facility there containing the MSR that was earlier used for MEG studies became

the main laboratory of the MEGMRI project in Finland. First, a test system was built, with a less extensive sensor coverage (eight sensors divided in three sensor modules). The test system used SQUID sensors that were concurrently developed by VTT Technical Research Centre of Finland and Aivon Oy. The first test-system ULF-MRI images of a water sample were obtained in August 2010 with a prepolarization field of B_p = 4 mT, and a measurement field of B_0 = 43 μT (Larmor frequency f_0 = 1.8 kHz). These images are the basis of Publication V; the theory, analysis and writeup were completed mainly during 2011. Subsequently, Publication IV was compiled in 2012.

Reflecting back on 2010, as an alternative line to using SQUIDs, mixed sensors based on giant magnetoresistance (GMR) were being developed in Saclay, France as a part of the MEGMRI project. The LF-MRI device that was developed there had one channel with a filling factor adequate to image *e.g.* small fruit. The LF-MRI system was operated in a constant field of B_0 = 8 mT (f_0 = 340 Hz) to obtain a sufficient SNR and to avoid the rapidly increasing $1/f$-noise in lower fields, *i.e.* at lower frequencies. Publication III was established at that time.

Back in Finland, the first successful NMR measurements with the final MEG-MRI prototype were made in June 2011 and brain images followed in October 2011: spin-echo, imaging time 35 min, resolution 6 mm × 6 mm, slice thickness (THK) = 10 mm, B_p= 15 mT (applied for 1 s at a time), B_0 = 50 μT (f_0 = 2 kHz), echo time T_E= 80 ms, maximum gradient amplitude 85 μT/m, field of view (FOV) 20 cm × 20 cm and SQUID magnetometer noise levels 4 fT/Hz$^{1/2}$.

The MEG-MRI prototype (see Fig. 1.1) is based on a commercial MEG device (by Elekta Oy) with a superconducting prepolarizing coil with one superconducting and another resistive compensation coil to minimize the stray fields at the MSR walls that would prevent the SQUIDs from measuring the subtle NMR signals. In addition, the SQUID sensors are tailored to tolerate especially the B_p field, and the dewar is surrounded laterally by the B_0 coils and G_x, G_y and G_z gradient coils. The radio-frequency (RF) transmit coil is positioned around the helmet, outside the dewar.

The MEG-MRI prototype was also validated as a tool for MEG. The first visual evoked fields (VEFs) were measured in December 2011. Later, it was found that dipoles fitted to VEFs recorded by the prototype matched with ones measured with the commercial MEG device (102 detector modules with one magnetometer and two orthogonal planar gradiometers, *i.e.* 306 detectors) in the BioMag Laboratory for the same subject. However, still, a limited number (approximately 20) of sensor modules (with the same pickup loop layout as in the MEG device in the BioMag Laboratory giving approximately $3 \times 20 = 60$ sensors in total) have been fabricated for the sensor helmet, making it challenging to have whole-head coverage; the other, more rigid reason for limited head coverage is that the niobium (Nb) shields used to protect the

Figure 1.1. The MEG-MRI prototype at Aalto University.

SQUID chips in the sensor modules tend to become magnetized, when the B_p field is applied. Therefore, the modules are positioned in the area of the visual cortex so they are approximately collinear with the B_p field and are magnetized minimally, yet allow VEF studies and ULF-MR imaging of the corresponding parts of the brain. However, whole-head coverage is desired but left for future work with sensor development.

Continuing from the end of 2012, the year 2013 was mainly characterised by making MEG measurements, developing the theoretical approach and performing signal analysis for Publication VI. The research problem was initially to detect whether high-frequency oscillations (HFOs) were nested with alpha waves. Proof of this was not found, but the work resulted in a method for analysing power correlations (PCs) between brainwaves. By the beginning of 2014, the writeup describing the PC method with simulations and experiments in Publication VI was completed.

1.3 Objectives and scope

The work that was done in the above framework resulted in the six publications that are presented in this Thesis. In brief, they were aimed at developing new ULF-MRI (microtesla-range, with prepolarization, $f_0 < 10$ kHz, applying SQUID sensors), LF-MRI (millitesla-range, 10 kHz $\lesssim f_0 \lesssim$ 500 kHz, applying GMR mixed sensors) and MEG methods (applying SQUID sensors). The specific aims of each of the publications I–VI were:

I To examine the effect of the largest magnetic fields used in ULF MRI on magnetizable objects, *viz.* attraction and torque, for safety considerations.

II To improve the determination of the transverse relaxation time, signal ampli-

tude, precession frequency and phase in ULF-NMR experiments, useful in the case of low SNR.

III To explore GMR mixed sensors in LF MRI instead of SQUID sensors that are used in ULF MRI, because mixed sensors are especially tolerable to larger magnetic fields.

IV To propose and simulate a new encoding mechanism applicable in ULF MRI giving versatility to ULF-MRI hardware construction.

V To present a quantitative approach in ULF MRI and provide a new method for ULF-MRI sensor-reading and measurement-geometry calibration.

VI To develop a method for estimating the coupling delays of brainwaves in the cortex and demonstrate its applicability to MEG.

1.4 Dissertation structure

The dissertation comprises the following three important parts. In Theoretical Foundation, basic physics and signal processing are reviewed, together with sensor technology, conventional MRI, ULF MRI, LF MRI and MEG. In Results, each of the dissertation publications is briefly described pertaining to their specific aims. In Discussion, the implications of the publications are elaborated.

2. Theoretical Foundation

To understand the results of the Publications, basic physics and signal-processing related to MRI and MEG are presented.

2.1 Electromagnetism

The classical phenomena of electromagnetism are described by Maxwell's equations; effects of electromagnetic fields on electrical charges are characterized by the Lorentz force.

2.1.1 Maxwell's equations

In differential form, Maxwell's equations are

$$\nabla \cdot \mathbf{E} = \frac{\rho}{\varepsilon_0} \tag{2.1}$$

$$\nabla \cdot \mathbf{B} = 0 \tag{2.2}$$

$$\nabla \times \mathbf{E} = -\frac{\partial \mathbf{B}}{\partial t} \tag{2.3}$$

$$\nabla \times \mathbf{B} = \mu_0 \left(\mathbf{J} + \varepsilon_0 \frac{\partial \mathbf{E}}{\partial t} \right) , \tag{2.4}$$

where $\mathbf{E}$ is electric field, $\mathbf{B}$ magnetic field, ρ charge density, ε_0 vacuum permittivity, μ_0 vacuum permeability, $\mathbf{J}$ current density and t time. Eq. (2.1) is known as Gauss's law, Eq. (2.2) Gauss's law for magnetism, Eq. (2.3) Faraday's law of induction and Eq. (2.4) Ampère's circuital law with the displacement current (last term) added by Maxwell [Jackson, 1999].

The law of Biot–Savart

As a consequence of Maxwell's equations in the steady state, there is the law of Biot–Savart

$$\mathbf{B}(\mathbf{r}) = \frac{\mu_0}{4\pi} \int \frac{I d\mathbf{l}' \times (\mathbf{r} - \mathbf{r}')}{|\mathbf{r} - \mathbf{r}'|^3} , \tag{2.5}$$

where $\mathbf{r}$ is the position, $\mathbf{r}'$ the position on the integration path with elements $d\mathbf{l}'$ and I is the electric current.

2.1.2 Lorentz force

Apart from Maxwell's equations, the equation for Lorentz force is

$$\mathbf{F} = q_c(\mathbf{E} + \mathbf{v} \times \mathbf{B}) \,, \tag{2.6}$$

where q_c is the charge of a particle moving with velocity $\mathbf{v}$ in an electric field $\mathbf{E}$ and magnetic field $\mathbf{B}$.

2.2 Fourier transform

The Fourier transform is defined by

$$\widehat{f}(\omega) = \int_{-\infty}^{\infty} f(t) e^{-i\omega t} \, dt \,, \tag{2.7}$$

where t can be *e.g.* time and $\omega = 2\pi\nu$ angular frequency. $f(t)$ is the time-domain representation of the function and $\widehat{f}(\omega)$ the function in frequency domain. The imaginary unit i is defined by $i^2 = -1$. The inverse Fourier transform is correspondingly

$$f(t) = \frac{1}{2\pi} \int_{-\infty}^{\infty} \widehat{f}(\omega) e^{i\omega t} \, d\omega \,. \tag{2.8}$$

The transform can be generalized straightforwardly to higher dimensions and can be applied in a short-term fashion (finite integration limits), whereby periodicity in the frequency space results. If the most rapidly oscillating signal component has frequency ν_{max}, according to the Nyquist–Shannon sampling theorem the sampling frequency has to be $\nu_s \geq 2\nu_{max}$ to avoid aliasing (signal components with different frequencies folding irreversibely on each other). There exists, however a method to circumvent this limitation for sparse signals based on random sampling [Donoho, 2006] (for a more practical approach, see [Lustig et al., 2007]).

2.2.1 Fourier transform point-spread function

In a finite Fourier transform, the spectrum does not have infinite resolution. For instance, when a sinusoid is Fourier transformed, the resulting peak in the frequency domain is not an impulse but has a certain width. This spread peak is called the point-spread function (PSF) which can be generalized to higher dimensions.

2.3 Sensor technology

There are several types of sensors for magnetic field measurements (see Table 2.1). The two ultra-sensitive superconducting sensors essential in this work are the SQUID

Table 2.1. Main types of sensors (magnetometers) sensitive to weak magnetic fields. In $^{(*)}$, f stands for frequency, and in $^{(\#)}$, k_B the Boltzmann constant, Θ the absolute temperature and R coil resistance (see [Nyquist, 1928]).

	Operation	Noise
Faraday coil (Eq. (2.3))	Signal $\propto f$ $^{(*)}$	$\sqrt{4k_B\Theta R}$ (V/Hz$^{1/2}$) $^{(\#)}$
Hall sensor [Lenz, 1990]	0 Hz to 1 MHz	10^{-7} T
Fluxgate [Ripka, 2003]	0 Hz to 10 kHz	10^{-11} T
Mixed sensor [Pannetier et al., 2005]	10 kHz to 1 GHz	10^{-14} T/Hz$^{1/2}$
DC SQUID [Clarke and Braginski, 2004]	0 Hz to 1 GHz	10^{-15} T/Hz$^{1/2}$
Atomic magn. [Dang et al., 2010]	0 to 100 Hz	10^{-16} T/Hz$^{1/2}$

sensor and the GMR mixed sensor. Both of them make use of superconductivity with either low-critical-temperature (low-T_c, in liquid helium (He), 4.2 K or −269°C) or high-T_c (in liquid nitrogen, N_2, 77 K or −196°C) materials. The existence of superconductivity depends on material, temperature, magnetic field and electric current.

2.3.1 Superconductivity

Superconductivity was discovered at liquid helium temperatures in 1911 [Onnes, 1998, van Delft and Kes, 2010]. Of key importance are the quantum-mechanical phenomena of flux quantization in a superconducting loop [London and London, 1935, London, 1948], found experimentally in 1961 [Deaver, Jr and Fairbank, 1961, Doll and Näbauer, 1961], and tunneling [Josephson, 1962, 1974]. According to the London equations, a superconductor is a perfect diamagnet, expelling an externally applied magnetic field. This is achieved by supercurrents flowing on its surface. The London equations were followed by the Ginzburg–Landau theory [Ginzburg and Landau, 1950, Ginzburg, 2004] that was expanded from Type-I superconductors to Type-II superconductors [Abrikosov, 1957] and the Bardeen–Cooper–Schrieffer (BCS) theory [Cooper, 1956, Bardeen et al., 1957a,b]. The BCS theory reduces to the Ginzburg–Landau theory close to the critical temperature [Gor'Kov, 1959]. They were able to give a microscopic theory for superconductors, explaining their phase transitions. A perferct superconductor is a perfect diamagnet with a magnetic susceptibility $\chi = \mu_r - 1 = -1$, where $\mu_r = 0$ is the relative permeability, expelling all magnetic fields from within. The Meissner effect is of key importance here: magnetic fields applied on a superconductor cause circulating electric supercurrents in it so that the external magnetic field is counteracted.

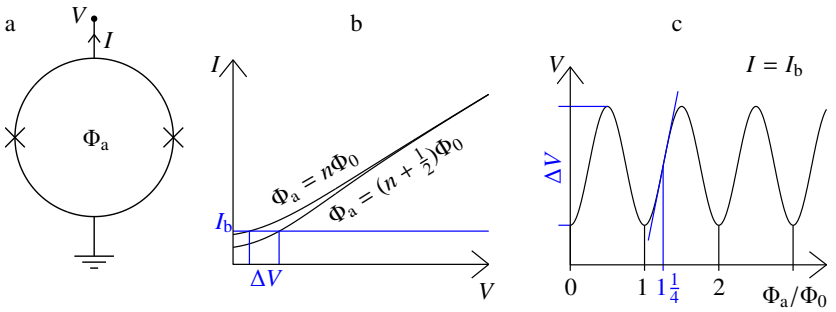

Figure 2.1. Physics of a DC SQUID. In a, the circuit design of a DC SQUID is given with the Josephson junctions denoted by the two crosses. I is the current passed through the SQUID loop and V the measured voltage. Φ_a is the magnetic flux penetrating the SQUID loop. In b, the I–V characteristics are given for two values of applied flux Φ_a; n is an integer. At a selected bias current I_b, the voltage difference between the two flux values is ΔV. In c, the periodic behaviour of the voltage V dependent on the applied flux Φ_a at a fixed bias current I_b is shown. The range of the voltage is given by ΔV which is also described in panel b. In DC-SQUID detectors, the flux penetrating the loop is fixed by a negative feedback to the linear part of the modulation curve in panel c (in this example, at $\Phi_a = 1\frac{1}{4}\Phi_0$). This enables measurement over a large dynamic range and bandwidth (see Table 2.1).

2.3.2 SQUID sensors

A schematic representation of the basic physics behind a direct-current (DC) SQUID (see *e.g.* [Clarke and Braginski, 2004]) applied in this work is shown in Fig. 2.1. The superconducting SQUID loop is interrupted by two Josephson junctions that can be resistive materials or constrictions through which the Cooper pairs (a pair of electrons) can tunnel. When a bias current I is passed through the SQUID, the voltage V is zero below the critical current of the Josephson junctions (I_c). When $I > I_c$, a change in the magnetic flux ($\delta\Phi_a$) through the SQUID loop produces a change in the measured voltage (δV), which is explained by the phase difference of the supercurrents in the superconductors on either side of the Josephson junctions. The phase dependency of the supercurrents makes the flux through the SQUID loop quantized (flux quantum $\Phi_0 = h/2e = 2.07{\cdot}10^{-15}$ Wb, where $h = 6.626{\cdot}10^{-34}$ Js is the Planck constant and $e = 1.602 \cdot 10^{-19}$ C is the elementary charge). When a constant bias current $I_b > I_c$ is passed through the SQUID, the Φ_a–ΔV characteristic shows a period of Φ_0 in the voltage ΔV alteration. In a DC-SQUID sensor, a flux transformer is used to enhance the field sensitivity with a magnetometric or gradiometric pick-up loop. The DC SQUID is typically operated with a flux-lock loop which fixes Φ_a by a negative feedback to a value where $\delta V/\delta\Phi_a$ is maximum. For a comparison of the noise characteristics of SQUID *vs.* Faraday coil detection, see [Myers et al., 2007]. The RF SQUID is different from the DC SQUID in that it has only one Josephson junction and the magnetic flux penetrating it is measured with the help of an external inductively coupled tank circuit (see *e.g.* [Clarke and Braginski, 2004]).

Shielding

In ULF MRI, despite the ultra-low fields, it is necessary to add extra protection to the SQUID sensors. Positioned in the pickup loop or the flux transformer, flux dams (a series of Josephson junctions) which become resistive with large currents, protect the SQUIDs from excessive fields [Clarke et al., 2007]. In addition, the SQUIDs can be shielded from the applied fields by over- and underlaid niobium plates [Luomahaara et al., 2011], or *e.g.* by enclosing the SQUIDs in a lead (plumbum, Pb) shield [Zotev et al., 2007b]. The former additional shielding was used in the SQUIDs of Publication V, but the measurements in Publication II were carried out without any additional shielding of SQUIDs in an MCG device.

2.3.3 GMR mixed sensors

The mixed sensors [Pannetier et al., 2004] consist of a superconducting loop with a constriction and commonly four GMR [Baibich et al., 1988] yoke elements. The mixed sensors demonstrate a strong structure- and magnetism-dependent $1/f$-noise $n_{V,1/f}$, in terms of spectral voltage V,

$$n_{V,1/f}(f) = \sqrt{\frac{\gamma_\mathrm{H}}{N_\mathrm{c} f}} RI \,, \tag{2.9}$$

towards lower frequencies f with γ_H the Hooge constant, N_c the number of charge carriers, resistance R and current I [Pannetier et al., 2004]. Furthermore, at higher frequencies (hundreds of kilohertz), thermal noise arising from the thermal movement of charge carriers $n_{V,\mathrm{therm}}$ in the GMR elements dominates the $1/f$-noise and is given in terms of spectral voltage by

$$n_{V,\mathrm{therm}}(f) = \sqrt{4 k_\mathrm{B} \Theta R} \,, \tag{2.10}$$

where k_B is the Boltzmann constant and Θ the absolute temperature. In terms of sensor magnetic field, these noises can be expressed by

$$n_{B,1/f} = \frac{n_{V,1/f}}{G \delta_R R I} = \sqrt{\frac{\gamma_\mathrm{H}}{N_\mathrm{c} f}} \frac{1}{G \delta_R} \quad \text{and} \tag{2.11}$$

$$n_{B,\mathrm{therm}} = \frac{n_{V,\mathrm{therm}}}{G \delta_R R I} = \sqrt{\frac{4 k_\mathrm{B} T}{R}} \frac{1}{G \delta_R I} \,, \tag{2.12}$$

where G is the flux-transformer gain and δ_R the proportion of resistance change per magnetic field change [Dyvorne et al., 2009].

The GMR elements have a separated hard and soft magnetic layer with the shape of a yoke to avoid magnetic noise in the measurement of the GMR voltage with an induced sensing current (see Fig. 2.2). In the hard layer, the magnetizing field $\mathbf{H}_\mathrm{h} = \tilde{\mathbf{H}}$, and without external field, the magnetizing field in the soft layer $\mathbf{H}_\mathrm{s} = -\tilde{\mathbf{H}}$. When the external field is applied, so $\mathbf{H}_\mathrm{s} = \tilde{\mathbf{H}}$, the overall resistance will change according

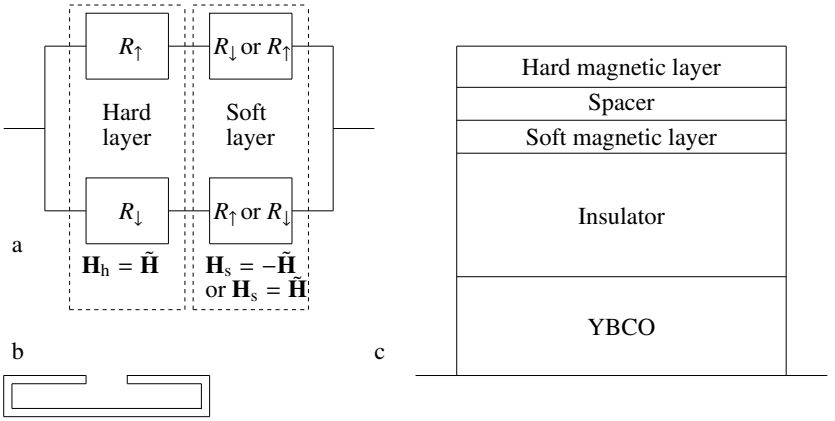

Figure 2.2. Physics of a GMR element. (a) Equivalent circuit of the GMR with spin-up resistance $R_\uparrow$ and spin-down resistance $R_\downarrow$ in magnetizing field $\pm\tilde{\mathbf{H}}$. (b) View of yoke shape perpendicular to the GMR stack. (c) mixed sensor epitaxy with the constriction (YBCO, or, yttrium barium copper oxide, and insulator) and the GMR stack (soft and hard magnetic layers with a spacer). The hard layer consists of two layers: a ferromagnetic one and an antiferromagnetic one. The latter helps the former to fix the magnetizing direction.

to

$$\Delta R = -\frac{1}{2}\frac{(R_\uparrow - R_\downarrow)^2}{R_\uparrow + R_\downarrow} \,. \tag{2.13}$$

Thus, it can be seen that the GMR effect in ΔR is the larger the bigger the difference between $R_\uparrow$ and $R_\downarrow$ is. The superconducting loop can be manufactured from a low-T_c material such as niobium (Nb), or a high-T_c material such as the YBCO compound (yttrium barium copper oxide, $YBa_2Cu_3O_{7-x}$). Around 10 Hz, GMR sensors with YBCO loops can have $1/f$-noise levels down to $\sim$ 100 fT/Hz$^{1/2}$ at 77 K and $\sim$ 30 fT/Hz$^{1/2}$ at 4 K [Pannetier-Lecoeur et al., 2010].

2.4 Conventional MRI

MRI is based on the NMR phenomenon of usually hydrogen nuclei (protons) in water (H_2O). A strong magnetic field ($B_0 \sim 1$ T) is used to polarize the nuclear magnetic moments, and in addition to the B_0 field, the sample is subjected in a desired manner to up to three orthogonal field gradients along with an RF field to encode the spatial information. When enough information is collected, the MR image is reconstructed, typically with the aid of Fourier transformations.

MRI is noninvasive and does not employ ionizing radiation. Volumetric imaging done with MRI has a soft-tissue contrast that is superior to CT, and it can be adjusted by modifying imaging parameters such as repetition interval T_R, T_E or flip angle α. Unlike ultrasound (US), MRI is not hindered by bones around the imaged target. In addition to direct diagnosis, MR brain images are important in *e.g.* EEG, MEG, TMS

and NIRS. Today, there are tens of thousands of MRI scanners in the world.

2.4.1 Quantum-mechanical basis of MRI

The most important particle in MRI is the proton that has a spin with spin angular momentum amplitude[1] $S = \hbar\sqrt{s(s+1)}$, where $s = 1/2$ is the principal quantum number; the projection quantum number in the direction defined as z is $s_z \in \{-s, -(s-1), \ldots, s-1, s\}$. The z component of the spin angular momentum of a proton is $S_z = s_z\hbar = \pm 1/2 \cdot \hbar$; in addition to S, only one component of the $\mathbf{S}$ vector can be measured at a time. The z component of a $s = 1/2$ particle is at the magic angle of $\theta_\mathrm{m} = \arccos(S_z/S) = \arccos(1/\sqrt{3}) \approx 54.7°$ with respect to the total angular momentum. In NMR spectroscopy, samples are spun at the magic angle to enhance line widths by averaging the time-dependent nuclear dipole–dipole interactions to zero. In an external field with amplitude B, the energy splitting due to the nuclear spin is given by[2] $E_{s_z} = -\mu B = -s_z\hbar\gamma B$, where $\mu = \gamma S_z = s_z\hbar\gamma$ is the spin magnetic moment. The alignment of spins is characterised by the Boltzmann distribution in temperature Θ. Let there be $N = N_\uparrow + N_\downarrow$ protons in total, with $N_\uparrow$ magnetic moment z components along $\mathbf{B}$ and $N_\downarrow$ against $\mathbf{B}$. In thermal equilibrium[3] $N_\downarrow/N_\uparrow = \exp\left(-\frac{E_{-1/2}-E_{1/2}}{k_\mathrm{B}\Theta}\right) = \exp\left(-\frac{\hbar\gamma B}{k_\mathrm{B}\Theta}\right)$. In practice, $\hbar\gamma B \ll k_\mathrm{B}\Theta$, whereby the spin-up and spin-down population difference can be approximated as

$$\Delta N = N_\uparrow - N_\downarrow \approx N\frac{\hbar\gamma B}{2k_\mathrm{B}\Theta}\,. \tag{2.14}$$

Hence, in a sample with N protons at temperature Θ, the net magnetic moment amplitude $|\mathbf{m}|$ at equilibrium is

$$|\mathbf{m}| = \Delta N \cdot |\mu| = N\frac{\hbar^2\gamma^2 B}{4k_\mathrm{B}\Theta}\,. \tag{2.15}$$

The fundamental equation describing the behaviour of a macroscopic magnetization $\mathbf{M}$ (density of aligned spin magnetic moments) is called the Bloch equation,

$$\frac{d\mathbf{M}}{dt} = \gamma\mathbf{M} \times \mathbf{B}\,, \tag{2.16}$$

given without relaxation terms for simplicity. The mechanical analogue is a spinning top with $\frac{d\mathbf{L}}{dt} = \mathbf{r} \times \mathbf{F}$, where $\mathbf{L}$ is the angular momentum, $\mathbf{r}$ describes the movement of the centre of mass and $\mathbf{F}$ is the force (gravity) acting on the spinning top. Using the Bloch equation, Eq. (2.16), it can be shown that in a constant external field $\mathbf{B}_0$, the macroscopic magnetization $\mathbf{M}$ precesses around $\mathbf{B}_0$ with an angular frequency of

$$\omega_0 = \gamma B_0\,, \tag{2.17}$$

[1] $\hbar = h/2\pi$ is the reduced Planck constant.
[2] $\gamma = 2\pi \cdot 42.58$ MHz/T $= 2\pi \cdot 42.58$ Hz/μT is the gyromagnetic ratio for protons (^{1}H).
[3] $k_\mathrm{B} = 1.38 \cdot 10^{-23}$ J/K is the Boltzmann constant.

when $\mathbf{M}$ is not parallel with $\mathbf{B}_0$. Thus, spin flips between the two proton states can be induced by RF quanta with frequency ω_0. In other words, when an external RF field is applied on the sample, its magnetization can be nutated by tuning the RF to ω_0. This is called nuclear magnetic resonance.

Longitudinal and transverse relaxation

The longitudinal relaxation time describes how the magnetization reaches a steady-state value. If the main field $\mathbf{B}_0 = B_0\hat{\mathbf{e}}_z$ is switched on at $t = 0$ with the magnetization (density of spins) $\mathbf{M}(0) = \mathbf{0}$, then

$$M_z(t) = M_{z,\infty}(1 - e^{-t/T_1}) , \quad t \geq 0 , \tag{2.18}$$

where $M_{z,\infty}$ is the equilibrium magnetization and T_1 the longitudinal relaxation time. On the other hand, if $\mathbf{M}(0) = \mathbf{M}_{z,\infty}$, and $\mathbf{B}_0$ is switched off,

$$M_z(t) = M_{z,\infty}e^{-t/T_1} . \tag{2.19}$$

Similarly to this equation, if there is a transverse component of the magnetization $M_{xy,0}$ at $t = 0$ in the same field $\mathbf{B}_0$,

$$M_{xy}(t) = M_{xy,0}e^{-t/T_2} , \quad t \geq 0 , \tag{2.20}$$

where T_2 is the transverse relaxation time. The transverse magnetization component $\mathbf{M}_{xy}$, however does not keep its orientation, but it rotates around $\mathbf{B}_0$. Considering the longitudinal and transverse relaxation processes, the Bloch equation (2.16) becomes

$$\frac{d\mathbf{M}}{dt} = \gamma\mathbf{M} \times \mathbf{B} - \frac{\mathbf{M}_{xy}}{T_2} - \frac{\mathbf{M}_z - \mathbf{M}_{z,\infty}}{T_1} , \tag{2.21}$$

where $\mathbf{M}_z$ is the z-directed part of $\mathbf{M}$, $\mathbf{M}_{xy} = \mathbf{M} - \mathbf{M}_z$ and $\mathbf{B}$ is allowed to be slightly perturbed from $\mathbf{B}_0$. Biological tissues have T_1's in the range of a second, and T_2's in the range of a hundred milliseconds in tesla-range MRI. The analysis with Eq. (2.21) can be simplified by converting into the rotating frame of reference, where the xy plane rotates round the z axis at the Larmor frequency.

Longitudinal T_1 relaxation characteristics

In tissue, T_1 gets longer with higher B_0 fields. The T_1 relaxation is affected by

Dominant: Dipole–dipole interactions (*e.g.* between two protons).

Lesser: Chemical shift anisotropy (impaired magnetic shielding because of non-spherical electron structures in molecules).

Weakest: Spin–rotation interactions (spin angular momentum *vs.* molecular rotation).

The T_1 relaxation happens in the direction of the static B_0 field. In the important

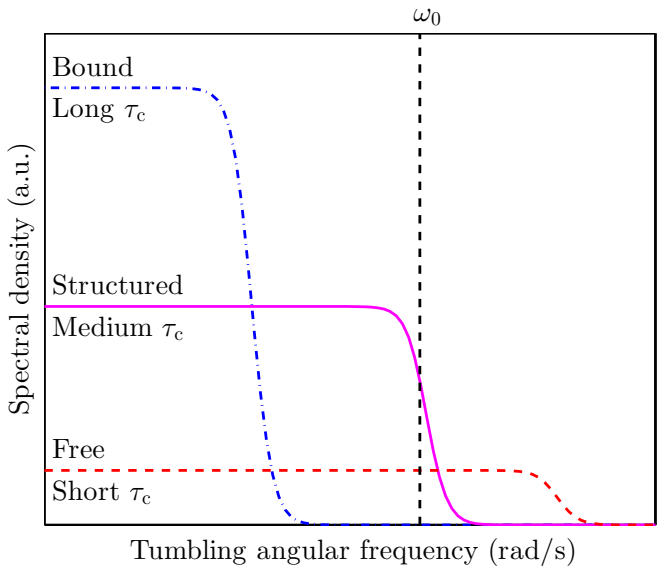

Figure 2.3. The effect of viscosity (bound, structured and free water with correlation time τ_c) on the spectral density of water molecule tumbling; the spectral density is in arbitrary units (a.u.). The more the water molecules move around (the more there is spectral density in a certain frequency band), the more the nuclear magnetization is affected; this shortens the relaxation times. At ω_0, structured water has a shorter T_1 than free water, giving the soft-tissue contrast. The relevant T_1's are often of the order of 1 s.

application of MR angiography, the T_1 time is reduced to an effective value $T_{1,\text{eff}}$ according to

$$\frac{1}{T_{1,\text{eff}}} = \frac{1}{T_1} + \frac{v}{\text{THK}}\,, \tag{2.22}$$

where v is the speed of blood through the imaging slice with thickness THK. Thus, $T_{1,\text{eff}}$ gives access to additional contrast in images with blood flowing in the vessels.

The spectral density of molecular tumbling of water molecules depends on the viscosity of water [Bloembergen et al., 1948]. As illustrated in Fig. 2.3, water with high viscosity (bound water) tumbles strongly at low frequencies (below MRI frequencies, long Brownian correlation time τ_c), water with medium viscosity (structured water) less strongly, but up to higher frequencies (even above MRI frequencies, medium τ_c), and water with low viscosity (free water) least strongly, but up to very high frequencies (above MRI frequencies, short τ_c). Thus, contrast can be achieved between different tissues, because they bind water in different ways. T_1 depends heavily on the environment of each water molecule; the more there is molecular tumbling, the shorter T_1 is, and *vice versa*.

Tranverse T_2 relaxation characteristics

In biological tissues, T_2 is likely to be affected by the same relaxation processes as T_1, *i.e.* magnetization transfer and other processes which take energy from the

spin system. In addition, T_2 depends on the macroscopic and microscopic inhomogeneities of the experienced magnetic field occurring at low frequencies. This is because the inhomogeneities lead to phase differences in the precession of the magnetic moments, which decreases the amplitude of the transverse sample magnetization. Thus, $T_2 \leq T_1$. With higher B_0 fields, T_2 gets shorter, because the low-frequency magnetic field anisotropies increase.

The free induction decay

Based on precession and T_2 relaxation, the basic signal (the FID) which can be observed in one detector

$$s(t) = Ae^{-t/T_2}\cos(2\pi f_0 t + \varphi)\,, \tag{2.23}$$

where the FID starts at time $t = 0$, A is the FID amplitude, $f_0 = \omega_0/2\pi$ is the Larmor frequency and φ is the signal phase (see Publication II). In experiments, the field inhomogeneity requires that T_2 is replaced by $T_2^* < T_2$ in Eq. (2.23).

2.4.2 Detection

In conventional MRI, the sensor of choice is the copper coil, making use of Faraday induction. The law of induction states that the voltage $u(t)$ in a coil depends on the flux $\Phi(t)$ penetrating the loop as $u(t) = \frac{d\Phi(t)}{dt}$. The sample magnetization $\mathbf{m}(t)$ at a certain location $\mathbf{r}$ affects the coil flux by $\Phi(t) = \mathbf{m}(t) \cdot \boldsymbol{\beta}(\mathbf{r})$, where $\boldsymbol{\beta}(\mathbf{r})$ is the lead field. Eventually, it can be seen that

$$u(t) = \frac{d\mathbf{m}(t)}{dt} \cdot \boldsymbol{\beta}(\mathbf{r}) \propto \omega_0 B_0\,, \tag{2.24}$$

where Eqs. (2.15) and (2.17) reveal the proportionality. Thus,

$$u(t) \propto B_0^2\,. \tag{2.25}$$

In other words, the sample polarization depends on B_0 and the precession frequency affects the voltage induced in the coil, and that also depends on B_0. The rationale behind building higher-field MRI devices is thus clear: doubling the field makes the detected voltage increase four-fold. However, there are challenges: higher fields mean higher RF frequencies that attenuate faster in tissue, affecting the uniformity of MR images, and also the specific absorption rate (SAR) must be taken into account carefully when strong RF pulses are delivered to the subject to avoid excessive tissue heating. Eventually, the magnetic coupling of the coil to the thermal noise of the imaged subject entails noise which increases proportionally to B_0 (see *e.g.* [Suits et al., 1998, Myers et al., 2007]), which reduces the SNR towards higher frequencies.

The MRI RF coils can be built separately for transmission and detection (Tx and Rx), or they can be combined as transceivers. To increase the sensitivity of the detection, the coils are tuned with a capacitor so that $1/\sqrt{LC} \approx \omega_0$ with coil inductance L

and tuned capacitance C. With a tesla-range field, and tuned bandwidth of the order of 500 kHz, the detected signals are in the range of tens of millivolts.

Quadrature detection

Traditionally, the two orthogonal components of the precessing magnetization are measured by quadrature detection: the signal band of each coil is demodulated from the $\omega \sim \omega_0$ range to the $\omega \sim 0$ kHz range with two channels by multiplying with either $\cos(\omega_0 t)$ or $\sin(\omega_0 t)$ and low-pass filtering [Liang and Lauterbur, 2000]. These make the two components of a complex sinusoid ($\exp i\varphi = \cos\varphi + i\sin\varphi$, neglecting amplitude).

2.4.3 Encoding methods

In NMR, the sample is kept in a homogeneous magnetic field so the NMR spectrum with chemical shifts is obtained. More advanced NMR may use higher-dimensional methods to determine protein structures; the dimensionality is determined by the number of varied inter-RF-pulse durations. Basic NMR reflects molecular composition, and the higher-dimensional methods allow for the determination of the spatial structure of molecules. In MRI, the key to producing images with information on the spatial distribution of tissues in the sample relies on using magnetic field gradients.

Frequency encoding

The frequency encoding gradient (G_ω) is of key importance. It modulates the precession frequency by perturbing the static field B_0 in some direction, say x:

$$\omega(x) = \gamma B_0 + \gamma G_x x \,, \tag{2.26}$$

where G_x is the gradient strength along the x axis; $B_0 \gg G_x x$ over the imaged object (FOV). If the magnetization at x is $M(x)$, the measured signal can be expressed as

$$s(t) = \int_x M(x) e^{-t/T_2} e^{i\gamma G_x x t + i\varphi} dx \,,\ t \geq 0 \,, \tag{2.27}$$

where the signal has been quadrature-detected (see Section 2.4.2) at $\omega_0 = \gamma B_0$, and the signal component x is in the real part $\mathrm{Re}\{s(t)\}$ and the signal component y in the imaginary part $\mathrm{Im}\{s(t)\}$. The amplitudes $M(x)$ can be recovered by the Fourier transformation

$$\begin{aligned} \hat{s}(\Omega) &= \int_0^\infty s(t) e^{-i\Omega t} dt \\ &= e^{i\varphi} \int_0^{t \gg T_2} \int_x M(x) e^{-t/T_2} e^{i(\gamma G_x x - \Omega)t} dx\, dt \,. \end{aligned} \tag{2.28}$$

The response for each x is maximum when $\Omega = \Omega(x) = \gamma G_x x$. The reconstructed one-dimensional magnetization image

$$|\hat{s}(\Omega(x))| \propto M(x) T_2 \,. \tag{2.29}$$

Phase encoding

In Eq. (2.28), there is an unused factor, $\exp(i\varphi)$, that allows phase encoding of MR data. Imagine that in y and z directions, there are additional gradients $G_{y,p'}$ and $G_{z,q'}$ applied for a duration of τ. Both gradients are stepped incrementally according to

$$G_{y,p'} = p'\Delta G_y\ ,\ p' \in \{-\lfloor P/2\rfloor, -\lfloor P/2\rfloor + 1, \ldots, -\lfloor P/2\rfloor + P - 1\} \text{ and } (2.30)$$

$$G_{z,q'} = q'\Delta G_z\ ,\ q' \in \{-\lfloor Q/2\rfloor, -\lfloor Q/2\rfloor + 1, \ldots, -\lfloor Q/2\rfloor + Q - 1\}\ , \quad (2.31)$$

where $\lfloor\cdot\rfloor$ denotes rounding down and ΔG_y and ΔG_z are the gradient increments such that $\gamma\Delta G_y\tau \times \mathrm{FOV}_y = 2\pi$ and $\gamma\Delta G_z\tau \times \mathrm{FOV}_z = 2\pi$, where FOV_y and FOV_z are the FOVs in y and z directions. Traditional phase encoding is achieved by stepping the y and z gradients at each repetition prior to acquisition. Now, the measured signal can be written

$$s(t, p', q') = \iiint_{xyz} M(x, y, z)e^{-t/T_2}e^{i\gamma(G_x xt + G_{y,p'}y\tau + G_{z,q'}z\tau)}\,dx\,dy\,dz\ , \quad (2.32)$$

where the phase in Eq. (2.28) has been assigned $\varphi = \gamma(G_{y,p'}y\tau + G_{z,q'}z\tau)$. The imaged volume FOV is discretized into $N \times P \times Q$ rectangular voxels of dimensions $\Delta x \times \Delta y \times \Delta z$, respectively. The discrete version of Eq. (2.32) with time step Δt reads

$$s(n', p', q') = \sum_{n,p,q} M(n, p, q)e^{-n'\Delta t/T_2}e^{i\gamma(nn'G_x\Delta x\Delta t + pp'\Delta G_y\Delta y\tau + qq'\Delta G_z\Delta z\tau)}\Delta x\Delta y\Delta z \quad (2.33)$$

that can be solved with the three-dimensional Fourier transformation to yield the MR image

$$|\tilde{s}(n, p, q)| \propto M(n, p, q)T_2\Delta x\Delta y\Delta z\ . \quad (2.34)$$

Thus, the smaller the voxel or the shorter T_2 is, the weaker the signal from the reconstructed voxel is.

RF pulses and slice selection

As noted in Section 2.4.1, RF pulses can be used to nutate or tilt the sample magnetization. Rewriting Eq. (2.21) in the rotating frame of reference, neglecting the relaxation terms that are slow compared to the duration of the RF pulse,

$$\frac{\partial \mathbf{M}'}{\partial t} = \gamma\mathbf{M}' \times \mathbf{B}'_{x'y'}\ , \quad (2.35)$$

where the prime refers to the coordinate system with rotating x and y axes. Now, imagine that an RF B_1 field $\mathbf{B}_1 = 2\hat{B}_1\cos(\omega_0 t)\hat{\mathbf{e}}_x$ is produced along the x axis in the laboratory frame. This field can be interpreted as the sum of two fields rotating with frequency ω_0 in opposite directions in the xy plane spanned by $\hat{\mathbf{e}}_x$ and $\hat{\mathbf{e}}_y$, *i.e.*, $\mathbf{B}_1 = \hat{B}_1\{[\cos(\omega_0 t)\hat{\mathbf{e}}_x + \sin(\omega_0 t)\hat{\mathbf{e}}_y] + [\cos(\omega_0 t)\hat{\mathbf{e}}_x - \sin(\omega_0 t)\hat{\mathbf{e}}_y]\}$. The field between the former brackets rotates at frequency ω_0, and is off-resonance with the magnetization rotating

at frequency $-\omega_0$ in the laboratory frame. The field between the latter brackets can be written in the frame rotating at $-\omega_0$ around the z direction as $\mathbf{B}_1'(t) = \hat{B}_1\hat{\mathbf{e}}_{x'}$, and fitting into Eq. (2.35) gives

$$\frac{\partial \mathbf{M}'(t)}{\partial t} = \gamma \hat{B}_1 \mathbf{M}'(t) \times \hat{\mathbf{e}}_{x'} \quad \text{with} \quad \mathbf{M}'(0) = M_0\hat{\mathbf{e}}_{z'} \quad \Rightarrow \tag{2.36}$$

$$\mathbf{M}'(t) = M_0[\sin(\hat{\omega}_1 t)\hat{\mathbf{e}}_{y'} + \cos(\hat{\omega}_1 t)\hat{\mathbf{e}}_{z'}] \,, \tag{2.37}$$

where $\hat{\omega}_1 = \gamma\hat{B}_1$ is the tilt-rotation angular frequency. Thus, $\mathbf{M}'(t)$ will be rotated around the x' axis by an angle α determined by the RF pulse amplitude and duration.

Slice selection is possible by applying a slice-selection gradient G_s on the sample. Then, if the gradient is applied in the z direction, the precession frequency

$$\omega = \omega_0 + \gamma G_\mathrm{s} z \tag{2.38}$$

and the RF pulse will tilt the magnetization at $z = 0$, because otherwise $\omega \neq \omega_0$, and the resonance condition is not satisfied. By variation of the RF pulse frequency, magnetizations at xy planes with desired z can be flipped. The thickness and uniformity of the selected slice can be controlled by varying the duration and modulating the amplitude of the RF pulse. An important shape for amplitude modulation is given by the sinc function ($\mathrm{sinc}\, x \sim \sin x/x$); because of the finite duration of the RF pulse, the sinc shape has to be apodized to finite length. With small flip angles, perfect sinc modulation would give uniform tilting within the slice and none elsewhere. The slice thickness behaves as

$$\mathrm{THK} \sim \frac{1}{\frac{\gamma}{2\pi}G_\mathrm{s}\tau} \,, \tag{2.39}$$

where τ is the duration of the RF pulse. Thus, a stronger gradient G_s gives thinner slices.

2.4.4 *k*-space

As can be seen from Eq. (2.33), the operation of imaging gradients plays an important role in the spatial encoding of MR images. To transform the collected data set from the measured k-space (space of spatial frequencies) into image space, discrete Fourier transformations are applied. If the phase in the complex exponential in Eq. (2.32),

$$\varphi(x, y, z) = \gamma[G_x x t + G_{y,p'} y\tau + G_{z,q'} z\tau] \,, \tag{2.40}$$

is rewritten as

$$\varphi(x, y, z) = 2\pi[k_x x + k_y y + k_z z] \quad \text{with} \tag{2.41}$$

$$k_x = \frac{\gamma}{2\pi}\int_0^t G_x(t')\,dt' \,, \tag{2.42}$$

$$k_y = \frac{\gamma}{2\pi}\int_0^t G_y(t')\,dt' \quad \text{and} \tag{2.43}$$

$$k_z = \frac{\gamma}{2\pi}\int_0^t G_z(t')\,dt' \,, \tag{2.44}$$

where G_x is constant in Eq. (2.42), $G_y(t') = G_{y,p'}$ is constant and integrated up to $t = \tau$ at each p' in Eq. (2.43) and $G_z(t') = G_{z,p'}$ is constant and integrated up to $t = \tau$ at each q' in Eq. (2.43). Now, the important relation between k-space and image space becomes clearer. In fact, all of the gradients in Eqs. (2.42) to (2.44) can be varied during acquisition. To avoid aliasing in an image with FOV $L_x \times L_y \times L_z$ and $N_x \times N_y \times N_z$ voxels, the k-space has to be sampled around the k-space origin up to spatial frequencies

$$\max(k_x) - \min(k_x) = \frac{N_x}{L_x}\,, \tag{2.45}$$

$$\max(k_y) - \min(k_y) = \frac{N_y}{L_y} \quad \text{and} \tag{2.46}$$

$$\max(k_z) - \min(k_z) = \frac{N_z}{L_z}\,. \tag{2.47}$$

2.4.5 Basic imaging sequences

In MRI, imaging sequences determine the way in which the data used for image reconstruction are collected. There are two principal methods: spin-echo (SE) and gradient-echo (GE) acquisitions. The sequences consist of blocks that are repeated (T_R) in a similar manner so that all of the relevant k-space is covered. The key idea of any echo imaging is to refocus the precessing spins at the echo time (T_E) after the start of the counteracted dephasing. Assuming that at locations ξ and $\xi + \delta\xi$ there are two spins experiencing a field described by $B(\xi) = B_0 + (G_1 + G_2)\xi$, the dephasing will develop as

$$\varphi(t) = \gamma B(\xi + \delta\xi)t - \gamma B(d)t = \gamma(G_1 + G_2)\delta\xi\, t\,, \quad 0 \le t < \frac{T_\mathrm{E}}{2}\,. \tag{2.48}$$

The inhomogeneity is described by the sum of two gradients $G_1 + G_2$, and is allowed to develop until $t = T_\mathrm{E}/2$, when the rephasing due to G_1 is initiated, so

$$\varphi(t) = \mp\gamma G_1\delta\xi\,\frac{T_\mathrm{E}}{2} \pm \gamma G_1\delta\xi\left(t - \frac{T_\mathrm{E}}{2}\right) + \gamma G_2\delta\xi\, t\,, \quad t \ge \frac{T_\mathrm{E}}{2}\,. \tag{2.49}$$

The upper $\mp$ and $\pm$ signs apply to SE and lower ones to GE. The echo peak is reached at $t = T_\mathrm{E}$, when rephasing is at its best, *i.e.* the dephasing because of G_1 is removed; the dephasing because of G_2 is not refocused.

Spin-echo sequences

Each block of the sequence is initiated at $t = 0$ by an excitation pulse by tilting the spins by an angle of $\alpha = \pi/2$ in a slice; the MR signal produced at this point is called the FID. After that, SE RF pulses [Hahn, 1950] can compensate for static field inhomogeneities (G_1 in Eq. (2.49)) that are present during the initiation of the echo up to the end of the echo [Carr and Purcell, 1954]; variable inhomogeneities

in the molecular environment and ones imposed by variable external fields cannot be rephased (G_2 in Eq. (2.49)). The RF pulse (see section 2.4.3) is given at time $t = T_E/2$ that rotates the spins through an angle of π. This turns the dephasing of the spins into rephasing, and at $t = T_E$, the peak of the echo is achieved. The echo peak decay depends on T_2 relaxation, while the decay omitting the refocusing π RF pulse depends on relaxation according to $T_2^* < T_2$. A popular application of SE is called turbo spin echo (TSE).

Gradient-echo sequences

Each block of the sequence is initiated at $t = 0$ by an excitation pulse by tilting the spins by a desired angle ($0 < \alpha \leq \pi/2$) in a slice. After that, GE pulses can compensate for field inhomogeneities caused by themselves (G_1 in Eq. (2.49)), but not other inhomogeneities (G_2 in Eq. (2.49)). At time $t = 0$, a gradient with amplitude G_1 is initiated; at $t = T_E/2$, the gradient is inverted to $-G_1$. The GE peak is observed at $t = T_E$. The GE peak relaxes according to T_2^*, and without the echo, the relaxation is even faster according to $T_2^{**} < T_2^*$. It is intuitive to think about the k-space, when GE is considered (see section 2.4.4). All of the essential k-space should be covered during the sequence. A popular application of GE is called echo-planar imaging (EPI) [Mansfield, 1977].

Signal spoiling

To speed up imaging, it may be desirable to spoil the remaining transverse magnetization. In gradient spoiling, a strong gradient is applied to the sample, resulting in dephasing of the transverse magnetization. In RF spoiling, several excitation pulses are given with different phases so that the transverse magnetization is cancelled. Gradient and RF spoiling can also be combined. RF spoiling can be applied in *e.g.* multi-slice imaging with short T_R, where the Ernst angle is used (see Section 2.4.7). The excitation pulse of $\pi/2$ is changed to $\alpha < \pi/2$, so part of the magnetization remains in the B_0 direction. However, to be able to repeat the low-angle excitation soon again, without artefacts, the remaining transverse magnetization is RF spoiled [Gras et al., 2013].

Backprojection

In the traditional backprojection method, a slice is selected, and the k-space is covered by letting the frequency-encoding gradient have all relevant directions within π rad. The reconstruction can be done with the help of (windowed) Fourier transformations, known as (filtered) backprojection. Each projection in the xy plane follows the equation

$$\mathcal{R}\{\rho_s(x,y)\}(p,\varphi) = \int_{-\infty}^{\infty}\int_{-\infty}^{\infty} \rho_s(x,y)\,\delta(x\cos\varphi + y\sin\varphi - p)\,dx\,dy\,, \qquad (2.50)$$

where $\mathcal{R}$ is the two-dimensional Radon transform, φ is the projection angle, $p = x\cos\varphi + y\sin\varphi$ is the scalar position in a certain projection, and the reconstruction is possible *e.g.* using Fourier transforms as stated by the projection-slice theorem [Liang and Lauterbur, 2000]. The backprojection method is essential in CT, but less used in MRI.

2.4.6 Parallel imaging

A key limitation to accelerating MR imaging has been the need to sample the k-space with a certain accuracy. If the k-space is undersampled below that, the reconstructed images are commonly aliased, *i.e.* some parts of each image are irreversibly overlaid. The application of compressed sensing is one solution to accelerate MR imaging [Lustig et al., 2007], and holds promise for *e.g.* faster three-dimensional angiography. However, parallel imaging is a more common approach.

In parallel imaging, an array of small receiver (Rx) coils, each sensitive to a small volume, is used. The k-space may be undersampled owing to the spatially independent information that the different coils convey, and aliasing is avoided. Typically $R_{\text{acc}} = 2$ to $R_{\text{acc}} = 4$-fold acceleration is commonly used by sampling $1/R_{\text{acc}}$ of the k-space. Subsequently, the SNR is reduced to $1/\sqrt{R_{\text{acc}}}$ of the unaccelerated one. To mention, four basic parallel imaging methods [Blaimer et al., 2004] are: partially parallel imaging with localized sensitivities (PILS [Griswold et al., 2000]) and sensitivity encoding (SENSE [Pruessmann et al., 1999]) that work in the image space, and simultaneous acquisition of spatial harmonics (SMASH [Sodickson and Manning, 1997]) and generalized autocalibrating partially parallel acquisitions (GRAPPA [Griswold et al., 2002]) that work in the k-space.

2.4.7 Image weighting

Structural MR images can be weighted primarily according to three parameters: the longitudinal relaxation time T_1, the transverse relaxation time T_2 (or the inhomogeneous transverse relaxation time T_2^*) and spin density ρ_{s}. The weightings are achieved by choosing appropriate T_{R}, T_{E} and α. For example, in a gradient-echo sequence, the intensity I_n of voxel n is given by

$$I_n = \rho_{\text{s},n} \frac{\left(1 - e^{-T_{\text{R}}/T_{1,n}}\right)\sin\alpha}{1 - e^{-T_{\text{R}}/T_{1,n}}\cos\alpha} e^{-T_{\text{E}}/T^*_{2,n}} , \tag{2.51}$$

wherein *e.g.* spin-density weighting is obtained when $T_{\text{E}} \ll T_2^*$ and either $\alpha \ll \alpha_{\text{Ernst}}$ or $T_{\text{R}} \gg T_1$ [Smith and Webb, 2011]. The Ernst angle (after Richard Ernst, 1991 Nobel Prize in Chemistry) gives maximal signal intensity: $\alpha_{\text{Ernst}} = \arccos[\exp(-T_{\text{R}}/T_1)]$.

Image contrast

The success of the excellent MRI contrast in soft tissue is based on the dependence of the tissue parameters (T_1, T_2 and ρ_s) on the occurrence of free- or structured-water protons in variable molecular environments in different tissues (see Fig. 2.3). Thus, also many pathological changes can be detected by adjusting the imaging sequence to an appropriate weighting of the tissue parameters. The sensitivity of T_2^* relaxation to tissue susceptibility changes is the basis of fMRI [Belliveau et al., 1991, Ogawa et al., 1992]: When a certain area in the brain is active, the concentrations of oxygenated (oxyhaemoglobin, Hb) and oxygen-depleted haemoglobin (deoxyhaemoglobin, dHb) change, which is detectable in blood-oxygen-level dependent (BOLD) weighted MR imaging as contrast changes. In such experiments, gradient-echo (echo-planar imaging) imaging is applied, because the full brain volume can be sampled in less than 1 s, and because the susceptibility changes produce better contrast in gradient-echo imaging than in spin-echo imaging.

There are two main kinds of contrast agents (CAs) that can be injected into the patient: positive (paramagnetic, based on gadolinium ions) and negative (superparamagnetic, based on iron oxide). The positive CAs reduce the longitudinal relaxation time T_1 to an effective value according to

$$\frac{1}{T_{1,\text{eff}}} = \frac{1}{T_1} + \alpha_1 c \,, \tag{2.52}$$

where α_1 is the T_1 relaxivity of the CA and c its molarity. These CAs are used to image especially the central nervous system for tumours. The negative CAs cause rapid T_2 relaxation in tissue, resulting in signal loss. They are used to image *e.g.* liver disease. The use of fluorine as a CA in imaging blood vessels has also been proposed (see *e.g.* [Ruiz-Cabello et al., 2011]).

Inversion recovery

Tissue weighting can also be achieved with the inversion recovery method. The imaged target is given a π pulse, whereafter recovery of the inverted magnetization is interrupted with an excitation pulse at a specific moment. Assuming that tissue A has a longitudinal relaxation time of $T_{1,A}$ and tissue B of $T_{1,B} \neq T_{1,A}$. Before the excitation pulse, the magnetization recovers as $M(t) = M_0[1 - 2\exp(-t/T_1)]$, $t \geq 0$. If the excitation is given at $t = T_{1,A} \ln 2$, the magnetization of tissue A will be zero, whereas tissue B produces a signal. Thus, this method can cancel the signal from unwanted tissues, if the longitudinal relaxation time of the unwanted tissues is different from the tissues of interest.

2.4.8 Image quality

The quality of an (MR) image can be characterised quantitatively through the SNR and the contrast-to-noise ratio (CNR). They may be defined as

$$\text{SNR} = \frac{\hat{I}}{\sigma_\text{n}} \quad \text{and} \tag{2.53}$$

$$\text{CNR} = \frac{|I_\text{B} - I_\text{A}|}{\sigma_\text{n}}\,, \tag{2.54}$$

where $\hat{I}$ is the desired-signal amplitude (*e.g.* image grayscale value in a target pixel), σ_n is the background noise standard deviation, and I_A and I_B are pixel grayscale values of tissues A and B, respectively.

2.4.9 Devices for conventional MRI

Both the installation costs and the operation of conventional MRI devices require significant investments. This will be apparent from the following considerations.

In an MRI experiment, the subject lies within the device (weight of the order of 10 tons, imaging bore diameter approximately 70 cm) in a strong magnetic field B_0, typically 1.5 or 3 T. Additional field gradients in the three spatial directions (G_x, G_y and G_z) are used, together with RF pulses (B_1) at frequency $\omega \sim \omega_0 = \gamma B_0$, are used for excitation and spatial signal encoding. The B_0 coil operates with superconducting wiring (in cryogenics), while the RF transmission and detection is achieved with tuned copper coils with signals in the mV range. The measurements are controlled by a modern computer capable of thousands of fast Fourier transformation (FFTs) reconstructions per second. The MRI device is positioned in an RF-shielded room to damp incoming or outgoing RF disturbances. Highly qulified personnel are required for the safe and efficient operation of the device.

Main coil structure

The main coil producing the B_0 field has thousands of windings of niobium-titanium (Nb-Ti) wire in liquid helium at 4.2 K. The superconductor carries a current of 100 to 300 A with measurement-wise deviations of the order of $1 : 10^9$, aided by superconducting and resistive shim coils [Smith and Webb, 2011]. To limit the fringe (stray) field at room walls to near 1 gauss = 0.1 mT, the main superconducting coil has a specific design. To ensure the controlled precession of the magnetization, the B_0 field is kept as homogeneous as possible, down to a few parts per million (ppm) [Liang and Lauterbur, 2000] which translates to a few microtesla. This is achieved with the shimming coils.

Gradient coils

The gradient coils create deviations in the imaging field in the direction of the B_0 field that can be controlled in the three orthogonal spatial directions. Within the imaging volume, the uniformity of the field gradients is usually close to 95% [Smith and Webb, 2011] with maximum strengths of the order of 50 mT/m, allowing resolutions down to 0.1 mm. The gradient coils can be actively shielded with additional coils to limit eddy currents induced in the cryogenic radiation shields further from the imaging bore. The z gradient (in the direction of the bore axis) is produced with a Maxwell coil, whereas the transverse (x and y) coils are saddle coils. The gradient slew rates (rates of switching) reach up to 200 T/m/s with a rise time typically less than 1 ms; the Lorentz forces (see Section 2.1.2) generated in B_0 make the MRI device structure vibrate, causing acoustic noise above 100 dB, so earplugs and headphones are mandatory. In clinical MRI, resolutions of 1024 pixels in a direction are feasible.

RF coils

For the RF coils, fewer large transmit (Tx) coils to minimize inductance can be used, whereas many smaller receive (Rx) coils to minimize noise and achieve parallel imaging are convenient. Alternatively, the same set of coils can be used as a transceiver (Tx/Rx). In parallel imaging, up to 100 coils can be combined in phased arrays. In body coils, the Tx power can go up to 35 kW. The Tx and Rx coils are tuned to the Larmor frequency by capacitors (see Section 2.4.2). The challenge with an MRI phased array is how to decouple the adjacent coil elements to cancel problematic interactions. This has been achieved *e.g.* by partial overlap of adjacent coils and low-impedance preamplifiers [Roemer et al., 1990]. It is noteworthy that there is no need for decoupling in ULF MRI when an array of untuned SQUID sensors is used. For whole-body imaging in conventional MRI, cylindrical coils embedded around the bore can be used, whereas in knee imaging, the birdcage coil is appropriate. Brain and surface imaging can be done with arrays of coils.

2.4.10 Safety

The strong B_0 field with its gradients attracts ferromagnetic objects that are therefore not allowed inside the imaging room. The B_0, B_1 and gradient fields may disturb medical implants. Thus, people with *e.g.* surgical clips or pacemakers are not allowed to be imaged if the implants are not MRI safe; most modern implants (including surgical clips and pacemakers) are MRI safe. The imaging sequence must be kept safe: too rapid gradient switching may cause peripheral nerve stimulation (PNS), and too frequent B_1 pulses may heat tissue above the SAR limits for tissue. When the

safety guidelines are followed, MRI is very safe.

2.5 Ultra-low-field MRI

The substantial differences between conventional and ULF MRI stem from the amplitude of the B_0 field used. In conventional MRI, it is of the order of 1 T ($f_0 \gtrsim 40$ MHz), whereas in ULF MRI, it is from 1 μT ($f_0 \gtrsim 40$ Hz) [Hilschenz et al., 2013] or even below to near 200 μT ($f_0 \lesssim 90$ kHz) [Clarke et al., 2007]. As was pointed out, in conventional MRI, Faraday induction is utilized, whereby the signal is proportional to B_0^2 (Eq. (2.25)). Without prepolarization, the signals in SQUID-detected ULF MRI [Luomahaara et al., 2011] (detection with an atomic magnetometer has also been demonstrated [Savukov et al., 2009]) would be proportional to B_0; prepolarization [Macovski and Conolly, 1993, Matter et al., 2006] in a field B_p that is often 1000-fold compared to B_0 [Burghoff et al., 2007, Zotev et al., 2007b], renders also the SNR 1000-fold. While prepolarization is mundane in ULF MRI, the use of dynamic nuclear polarization (DNP) has not been common, although Overhauser DNP has been successfully performed [Zotev et al., 2010]. For a review on ULF MRI, see [Espy et al., 2013].

2.5.1 Magnetically shielded room

MSRs [Mager, 1970] can be characterised according to their response to the external fields of different frequencies. The fact that metallic materials have different permeabilities and conductances is utilized in the design of MSRs. For the purpose of MEG, the low-frequency (below a few hertz, down to DC) field disturbances can be suppressed with typically two or more layers of high-permeability (relative permeability of the order of 10^5) ferromagnetic material (often 1-mm-thick mu-metal [Jiles, 1998]). In MEG and also in ULF MRI, the higher-frequency (up to the kilohertz range) disturbances are suppressed with one or more layers of well-conducting material (up to 10-mm thick aluminium) [Burghoff et al., 2007, Zevenhoven et al., 2014]. As required by MEG, both methods are used for noise suppression in MEG-MRI [Burghoff et al., 2009, Matlashov et al., 2012, Vesanen et al., 2013a]. The high-permeability material becomes magnetized by low-frequency external fields, opposing them, whereas in the well-conducting material, eddy currents are induced by the higher-frequency fields so that the higher-frequency fields are also suppressed. In addition to this passive shielding, the MSR can be surrounded with coils, allowing active cancellation of ambient magnetic fields [Cohen et al., 2002, Knappe-Grueneberg et al., 2008]. As pointed out in Section 2.5.2, the eddy-current shielding can pose

challenges with fields which are rapidly switched *within* the MSR in ULF MRI.

2.5.2 Magnetic fields

As in conventional MRI, it is commonly preferable to keep the B_0 field as homogeneous as possible also in ULF MRI. However, as it is the absolute requirement for homogeneity (approximately 1 μT) that matters, ULF MRI homogeneity can be of the order of 0.1 to 1% instead of nearly 1 ppm in conventional MRI (see Section 2.4.9). For spectroscopic measurements, even better homogeneity may be required. In a 1.8-μT field, a line width of 1 Hz for mineral oil was reached with a 1% homogeneity [McDermott et al., 2002], while a study down to the nanotesla range revealed a line width of below 0.2 Hz for distilled water with an inhomogeneity below 0.1% [Burghoff et al., 2005]. In these kinds of applications, advanced analysis methods to determine the FID signal parameters are useful, especially if the FIDs oscillate slowly and over a short period, because simple analysis may produce biased results in the presence of noise (see Publication II).

Prepolarization

In MRI, prepolarization has been used earlier in imaging in the Earth's field [Stepišnik et al., 1990] and also in imaging with electromagnet fields (proposed *e.g.* in [Sepponen, 1990]) [Macovski and Conolly, 1993, Shao et al., 2002], before its application in SQUID-detected MRI [McDermott et al., 2004, Zotev et al., 2007a]. B_p is the strongest field in ULF MRI, and it is pulsed on and off during an imaging sequence (field cycling). The prepolarization duration is of the order of 1 s, and the acquisition period (prepolarization off) lasts typically less than 1 s. In a sequence, such a block is repeated until sufficient coverage of the k-space is gathered. To speed up imaging, it is often desirable to ramp B_p up and down rapidly. To avoid eddy-current buildup in the MSR walls [Vesanen et al., 2012], self-shielded B_p coils that zero the dipole, quadrupole or higher multipole components of the coil can be constructed [Nieminen et al., 2011]. Also, the MSR shielding, often made from aluminium (Al), which protects from external RF fields, can be structured so that the internally pulsed B_p cannot induce significant eddy currents in the aluminium plates [Zevenhoven et al., 2014]. Another recent development is the theory for dynamical cancellation that aims at suppressing specific spatiotemporal components of eddy currents by modifying the B_p time course [Zevenhoven, 2011]. B_p can also be switched through different values before acquisition to improve image contrast [Nieminen et al., 2013].

Concomitant gradients

The gradient fields used in ULF MRI are of the order of 100 μT/m. Compared to $B_0 \sim 100$ μT, the strong gradient fields make significant contributions to the imaging field as so-called concomitant gradients emerge [Volegov et al., 2005]. These gradients cause spatial deviations in direction of the measurement field, which complicates the precession of the magnetization across the sample. However, using advanced reconstruction methods, as in prepolarization encoding [Nieminen et al., 2010], it is possible to consider the concomitant gradient image artefacts and successfully reconstruct images [Myers et al., 2005, Nieminen and Ilmoniemi, 2010, Hsu et al., 2013].

Electronics

When the B_0 coil and gradient coils are operated during acquisition, very low-noise currents are needed. In addition, it may be necessary to ramp the fields rapidly. In the operation of the MEG-MRI prototype at Aalto University [Vesanen et al., 2013a], ramping during acquisition has been avoided and the currents have been supplied from batteries with regulators. An improvement is expected with the ultra-low-noise amplifier [Zevenhoven and Alanko, 2014] built at Aalto University which can already be used. The amplifier makes use of small- and large-voltage sources which can provide ultra-low-noise current and fast ramps, respectively.

2.5.3 ULF-MRI sensors

Low-T_c SQUIDs can be applied in ULF MRI for excellent SNR from near DC up to the kilohertz range, whereby in ULF MRI applications they are the most common sensors; succesful high-T_c SQUID ULF-MR measurements have also been conducted [Chukharkin et al., 2013]. Atomic magnetometers have also been used, approaching the SNR of SQUIDs [Savukov et al., 2009]. They have also been used in NMR prior to MRI (for a review, see [Greenberg, 1998]). The optimal arrangement of SQUID sensors has been earlier studied in MEG [Ahonen et al., 1993]. More recently, it has been shown that in an example setup, SQUIDs outperform inductive coils as detectors in terms of SNR up to a field of 250 mT [Myers et al., 2007]. Layouts of SQUID-sensors in commercial MEG devices allow a practical SNR, although improvements could be done [Zevenhoven and Ilmoniemi, 2011].

2.5.4 Image formation

In image formation, most of the methods used in conventional MRI (Section 2.4) are applicable. However, new phenomena may need to be taken into account (B_p field, concomitant gradients *etc.*, see Section 2.5.2), but also flexible usage of the imaging

fields allows for new possibilities. For example, in addition to frequency and phase encodings, a new encoding method entitled gradient-excitation encoding (GEE) has been proposed (Publication IV). However, these simulations did not encompass concomitant gradients which may cause complications in the image reconstruction.

Tolerance for susceptibility variations and eddy currents

In conventional MRI, susceptibility variations of tissues change the MR signals, which is in fact the basis of fMRI (see Section 2.4.7). However, often the susceptibility variations lead to image artefacts (*e.g.* tissue *vs.* air cavities in the head). ULF MRI is not sensitive to susceptibility variations and, in addition, the lower frequency of the RF pulses and the smaller-amplitude ramped gradient fields enable imaging *e.g.* through a metallic beverage can [Mößle et al., 2005].

Parallel imaging

The application of an array of SQUID sensors opens the possibility for parallel imaging in ULF MRI. The methods used in conventional MRI (see Section 2.4.6) are applicable but in case of low SNR, may not lead to considerable acceleration. However, parallel ULF MRI has been demonstrated with SENSE reconstruction; correction of concomitant gradient artefacts is also made [Zotev et al., 2008].

Quantitative imaging

A careful modelling and analysis of ULF-MRI measurement set-ups makes it possible to estimate ULF-MR images quantitatively. This allows *e.g.* calibrating the set-up or enables imaging tissue water content, where susceptibility variations prevent it in conventional MRI (see Publication V). In SQUID systems for MEG, the sensor calibration is commonly done with an array of small circular coils [Pasquarelli et al., 2004] or triangle current phantoms [Oyama et al., 2011], which could thus be circumvented in MEG-MRI.

Direct neural imaging

It has been suggested that the neuronal currents in the brain might be sufficiently large to enable direct neural imaging (DNI) [Kraus, Jr et al., 2008, Körber et al., 2013]. The method would be based on the small variable neural currents whose minute magnetic fields could alter the precession of the nuclear spins in ULF MRI. A similar method, current density imaging (CDI), has been proposed to determine *e.g.* sample conductivity by passing a weak current through it in ULF MRI [Nieminen et al., 2014, Vesanen et al., 2014].

2.5.5 Safety

Compared to safety considerations in conventional MRI (see Section 2.4.10), ULF MRI is easier, particularly because of the lack of a strong B_0 field. The low fields make the operation of the ULF-MRI device silent because of the absence of large Lorentz forces (see Section 2.1.2), and the feeling of claustrophobia is mitigated owing to the bore-free structure. Regarding the projectile danger, even elongated ferromagnetic objects are only weakly attracted, and only large ferromagnetic implants may experience a torque which could cause some pressure on tissue (Publication I). The dependency of magnetization on object shape is called demagnetizing.

Demagnetizing factors

When magnetizable objects that are magnetically soft (*i.e.*, lose their magnetization when removed from the magnetic field) are subjected to a magnetic field, their magnetization depends on their shape. This dependency is known as demagnetizing. In Publication I, the demagnetizing factors in the well-known case of spheroidal objects is handled, based on Maxwell's equations (see Section 2.1.1). In fact, even in the case of a general ellipsoid, exact demagnetizing factors can be derived [Osborn, 1945]. Also, approximative demagnetizing factors for cylinders have been derived [Chen et al., 1991].

2.6 Low-field MRI

LF MRI is categorised between ULF MRI and conventional MRI in terms of field strength $B_0 \sim 10$ mT ($f_0 \sim 100$ kHz). Because the B_0 field is of the order of B_p in ULF MRI (see Section 2.5.2), images with sufficient SNR can be obtained without prepolarization. Furthermore, with orders of magnitude larger f_0 compared to ULF MRI, sensors other than SQUIDs can be considered. To detect the femtotesla-level MR signals with sufficient SNR, conventional Faraday coils can be used, or alternatively GMR mixed sensors (see Section 2.3.3) [Pannetier et al., 2005]. GMR mixed sensors have an excellent field tolerance and recovery from RF pulses and show orders of magnitude lower noise than Faraday coils at biophysical frequencies (~ 30 fT/Hz$^{1/2}$ at 10 Hz at 4 K) [Pannetier-Lecoeur et al., 2010]. GMR mixed sensors can also be coupled to a pick-up loop, allowing for a larger FOV [Sinibaldi et al., 2013].

For example, MCG has been successfully performed with GMR mixed sensors [Pannetier-Lecoeur et al., 2011], as well as LF MRI (see Publication III) which could potentially be combined with *e.g.* MEG (see Section 2.7) in the future. LF MRI

can be considered safer than conventional MRI, similarly as ULF MRI (see Section 2.5.5), because of the moderate-strength magnetic fields.

2.7 MEG

The two currently known, millisecond-resolution methods for non-invasive brain mapping are EEG and MEG [Hämäläinen et al., 1993]. The first measurement of a brainwave, the alpha wave, was made by Hans Berger [Berger, 1929] by observing the electric voltage fluctuations at 10 Hz from the scalp. Subsequently, EEG has had a considerable impact on the knowledge of the function and structure of the brain [Niedermeyer and da Silva, 2005]. Advantages of EEG compared to MEG are that a magnetically shielded room is not needed in measurements, the lack of cryogenics and substantially lower operating cost. On the other hand, sources can be pinpointed more accurately by MEG particularly if an accurate presentation of head conductivity is not available. Both MEG and EEG are based on detecting neural currents, but MEG is more sensitive to primary currents tangential to the head (in the sulcal walls) whereas EEG sees both tangential and radial current components. It is estimated that 10 000 to 50 000 pyramidal neurons should be active simultaneously in MEG and EEG for detection [Murakami and Okada, 2006].

2.7.1 MEG sensors

Although low-T_c SQUIDs with noise near 1 fT/Hz$^{1/2}$ at 10 Hz are the most common sensors in MEG applications today, successful measurements have been conducted with an array of atomic magnetometers [Kim et al., 2014]. However, although the noise level with the array reached approximately 4 fT/Hz$^{1/2}$ at 10 Hz, the technical implementation with the atomic magnetometers is not yet mature. High-T_c SQUIDs with noise levels of approximately 50 fT/Hz$^{1/2}$ at 10 Hz have been used in a two-channel MEG measurement [Öisjöen et al., 2012]. However, an advantage over the noise was that it was possible to position the sensors very close to the head, approximately 2 cm closer than with state-of-the-art low-T_c SQUID array, giving an enhanced SNR.

2.7.2 Measurement interference suppression

In MEG, the measurements are contaminated by ambient magnetic fields, even within the MSR. Making use of the so-called signal-space projection (SSP) method [Uusitalo and Ilmoniemi, 1997], the interference can be suppressed [Parkkonen et al., 1999]. After a measurement of empty-room noise, the data are decomposed into

principal components, the most significant of which can be used in projecting out noise in an MEG measurement. Another method for noise suppression, signal-space separation (SSS) [Taulu et al., 2004] makes use of the spatial origin of the desired signals. The measurement is projected to two harmonic bases with components originating either within the sensor array (optimally the brain) or outside the sensor array. The denoised signals are calculated by inverting the measured sensor signals into the harmonic basis, selecting the components corresponding to the brain signals and reconstructing only these components back to the signal space.

2.7.3 Blind source separation

There exist several methods to improve the SNR of brainwaves. An important view in this is blind source separation (BSS) where the signals are sought for with only few assumptions, *e.g.* maximum variance or uncorrelatedness *etc.* In BSS, methods such as principal component analysis (PCA) [Pearson, 1901], projection pursuit [Friedman and Tukey, 1974], factor analysis [Reyment and Jöreskog, 1996] or independent component analysis (ICA) [Hyvärinen et al., 2001, 2010] have been used. Recently, the new BSS method of spatio-spectral decomposition (SSD) has been developed [Nikulin et al., 2011].

2.7.4 Forward and inverse problem

In MEG, the neuronal currents are regarded as sources which can, under favourable conditions, be detected with suitable sensors. Given a source current distribution, and calculating the sensor signals is called the forward problem; *vice versa*, the transformation from sensor space to source space is called the inverse problem [Sarvas, 1987, Mosher et al., 1999, Darvas et al., 2004]. The forward and inverse problems apply also in EEG (for a review, see [Grech et al., 2008]). In a head source model of spherically symmetric conducting layers, it can be shown that MEG is only sensitive to tangential current sources [Grynszpan and Geselowitz, 1973], whereas EEG is also sensitive to currens in other directions.

The concept of an equivalent current dipole (ECD) is an important tool in both MEG [Brenner et al., 1978] and EEG. The measured magnetic field or electric potential distribution can be fitted into one or more ECDs in an inverse problem solution. The inverse problem is ill-posed, because although any current disrtibution in the brain can be modelled with ECDs, it is always possible to find ECDs or combinations thereof that are not visible in the forward problem solution, and thus cannot be uniquely remapped in the inverse problem solution. The ECDs are considered as the primary currents generated particularly by the graded post-synaptic potentials

following action potentials in cells, and in tissue they are accompanied by the volume currents allowing the proper circulation of total current. In the spherically symmetric model, the MEG fields can be calculated by making use of the primary currents [Sarvas, 1987]. In EEG, the conductivity structure is also needed, as well as in non-spherical MEG models.

Solving the inverse problem

To find the source current distribution, minimum norm estimates (MNEs [Hämäläinen and Ilmoniemi, 1994]) can be used. The assumption that most of the MEG and EEG signals come from the cortex can also be used by tessellating the cortical surface and positioning a current dipole at each tessera. In this imaging approach, solving the amplitudes of the thousands of current dipoles requires regularization *e.g.* by the SVD [Gençer and Williamson, 1998].

To solve the inverse problem in MEG or EEG, also other methods have been developed [Baillet et al., 2001]. In the least squares method, the positions and amplitudes of a fixed number of ECDs can determined by using a nonlinear model, where the model error is minimized iteratively. In the beamformer approach, a spatial filtering matrix is formed to enhance the signal of a source at a chosen location. By traversing the relevant source space, a source image can be formed [Van Veen et al., 1997]. In the multiple signal classification (MUSIC) approach, the singular value decomposition (SVD) is applied to find the subspace where most of the signal lies. Subsequently, ECDs numbering the subspace dimension can be found one at a time, such that the ratio of the norm of their gains projected out of the subspace to the norm of the gains is minimum [Mosher et al., 1992].

2.7.5 Studying the brain

In MEG, the function of the human brain has been studied extensively with different methods [Hari and Salmelin, 2012]. As an example, mismatch negativity (MMN) is mentioned [Näätänen, 2001]. MMN is an alteration in the brain response to a deviant stimulus (usually auditory) which can be measured by EEG or MEG. On the other hand, the continuous activity of the brain can be observed in neuronal oscillations [Hari and Salmelin, 1997, Buzsáki and Draguhn, 2004, Hari and Salmelin, 2012]. Neural oscillations are often categorised according to the brain area they originate from and whether they are the neural correlates of some state of the brain, in addition to their frequency content. For example, with a strict definition, the alpha wave at 8 to 13 Hz is the most prominent brainwave, found in the visual cortex, whereas the mu wave has similar frequency content, but can be assigned to the motor cortex, both with different functions [Jones et al., 2009]. The coupling between different brainwaves

has been studied extensively with cross-correlations based on phase and amplitude [Le Van Quyen and Bragin, 2007, Tort et al., 2010, Onslow et al., 2011, Palva and Palva, 2012, Hipp et al., 2012]. A novel method suggests that millisecond-range coupling delays between brainwaves can be detected with a power cross-correlation method (Publication VI).

3. Results

The main results related to the research questions (Section 1.3) are presented.

3.1 Publication I: "Safety in simultaneous ultra-low-field MRI and MEG: Forces exerted on magnetizable objects by magnetic fields"

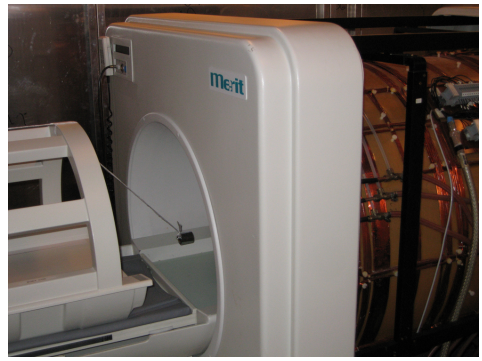

Figure 3.1. Experimental setup for measuring forces on magnetizable objects.

In Publication I, measurements (see Fig. 3.1) and theoretical predictions on magnetizable objects subjected to magnetic fields were made to find out whether the magnetic fields used in ULF-MRI measurements could pose safety issues. Using an existing 0.1-T system with a Helmholtz coil (maximum field 94.5 mT, coil radius 44.4 cm), it was found that magnetically soft, elongated objects align with the field, and in the area of the coil axis where the magnetic field gradient is strongest, objects with more elongation experience a larger force from the magnetic field in proportion to their weights. The crude approximation of a magnetically soft medical implant with length 5 cm and a square cross-section of 2 mm $\times$ 2 mm could produce a pressure of 2 atmospheres on tissue. Hence, it is safer if objects in the vicinity of the ULF-MRI device or medical implants in imaged patients are non-magnetic and not sharp.

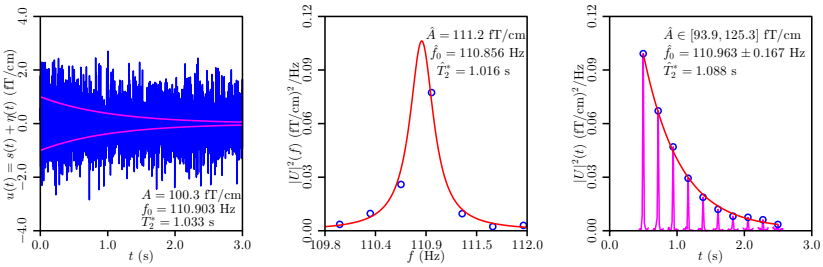

Figure 3.2. Illustration of determination of FID parameters by simulation. In the graph on the left, $s(t) = A\exp(-t/T_2^*)\cos(2\pi f_0 + \varphi)$ is the FID signal, whose envelope is indicated by the magenta curves, that is buried under noise $\eta(t)$. Estimates for the signal amplitude A, Larmor frequency f_0 and inhomogeneous transverse relaxation time T_2^* are obtained by the Lorentzian fit to the discrete power spectrum over the circular points in the middle graph. The graph to the right gives other estimates to the same parameters by the exponential fit to the power-spectral Lorentz peak decay in a moving time window. The phase φ can be estimated by other means.

3.2 Publication II: "Improved determination of FID signal parameters in low-field MRI"

In Publication II, methods for analysing the FID parameters in ULF NMR were developed (see Fig. 3.2). The methods are well suited for measurements that comprise only the real part of an oscillating signal, and have only a few samples representing the FID spectral peak. By observing the decay of the power-spectral Lorentz peaks which are computed in advancing time windows, it is possible to determine the transverse relaxation time. Making use of the relevant first integrals, an exponential with an additive constant is fitted to the peak heights. The signal amplitude and Larmor frequency are better accessible by fitting a Lorentzian shape to the power-spectral peak. These methods take the noise into account. Two methods for determining the signal phase were also presented, based either on the absorption and dispersion Lorentzians, or fitting a sinusoid to the data. It was found, however, that in noisy signals, determining the phase was more difficult than determining the transverse relaxation time, signal amplitude and Larmor frequency. Eventually, it was found that in the microtesla field, the inhomogeneous transverse relaxation time of the tap water sample was approximately 1.05 s.

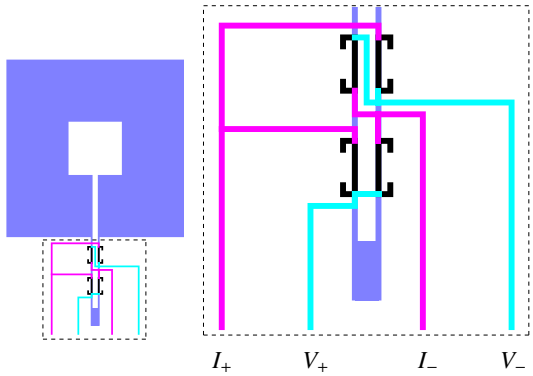

Black: GMR yokes, lengths 250 µm
Magenta: Sensing current
Cyan: Measured voltage
Blue: YBCO high-T_c loop
T_c = 80 K, gain ~ 716

B_0 = 8 mT (f_0 = 340 kHz)
G_{max} = 1.5 mT/m
B_0 homog. 10 ppm, G lin. 1%
FOV (6 cm)^3
Noise ~ 20 fT/Hz$^{1/2}$ @ f_0
Sensor–sample dist. 30 mm

Figure 3.3. GMR mixed sensor (left) with a blow-up of the constriction area (middle). Sensor characteristics and MR imaging parameters are given on the right.

3.3 Publication III: "Low field MRI with magnetoresistive mixed sensors"

In Publication III, GMR mixed sensors were used in LF MRI (see Fig. 3.3). The thermal noise (see Eq. (2.12)) of the sensor is of the order of 20 fT/Hz$^{1/2}$ which the $1/f$-noise (see Eq. (2.11)) reaches near 100 kHz. Thus, the LF-MRI application is feasible, and is demonstrated with a high-T_c flux-to-field transformer manufactured from the YBCO compound in superconducting state at 77 K in liquid nitrogen. The rather high Larmor frequency (f_0 = 340 kHz) enables imaging without magnetic shielding. The B_0 field was produced by a Helmholtz coil and three orthogonal gradients with an inverted Helmholtz pair and two figure-of-eight coils. The RF coil was wound around the sample. The acquisition was based on a gradient echo with THK ~ 2.5 mm, 128 phase-encoding steps and 20 repetitions averaged. The phantom measurements with variably $NiCl_2$-doped water compartments showed good contrast-to-noise ratio (CNR, see Eq. (2.54)) and a spatial resolution of the order of 1 mm^3.

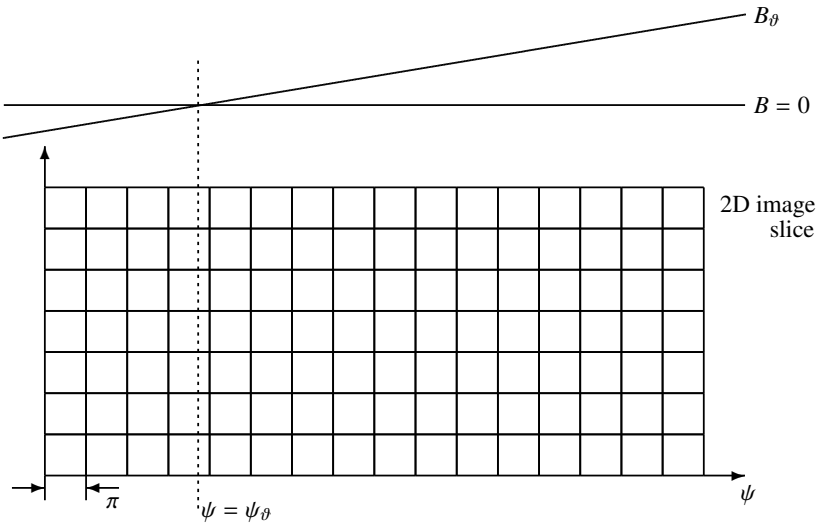

Figure 3.4. Variation of the GEE field with zero-crossing at $\psi = \psi_\vartheta$. The field (G_ϑ) has a constant gradient and is modulated with a broadband sinusoid. Thus, after the GEE, the acquired signal amplitude in the horizontal direction of the two-dimensional (2D) image slice is modulated stepwise so that when maximal GEE is applied, the signal amplitude in the voxels at the zero-crossing is not affected (signal amplitude multiplied by $\cos(\psi - \psi_\vartheta) \approx \cos(0) = 1$), whereas away from the zero-crossing, the amplitude is modulated by $\cos(\psi - \psi_\vartheta) \approx \cos(n\pi) = \pm 1$, where n is an integer. At intermediate GEE stages, the phase within the cosine is a fraction of $n\pi$. The signal decay within voxels requires a continuous inspection which is neglected for simplicity. With the suggested imaging sequence and reconstruction method, additional gradient-excitation encodings are necessary, if the zero-crossing $\psi = \psi_\vartheta$ is within the sample; the maximum is half of the voxel count in the GEE direction.

3.4 Publication IV: "Gradient-excitation encoding combined with frequency and phase encodings for three-dimensional ultra-low-field MRI"

In Publication IV, a novel spatial encoding method was proposed and tested by simulations. With the tested model, it was possible to reconstruct a three-dimensional image of a phantom with combined frequency, phase and GEE. In GEE, the sample is subjected to a gradient field from a coil that is driven with a broadband excitation current that is stepped between sweeps (see Fig. 3.4). The GEE field is perpendicular to the B_0 field, and the three encoding gradients are orthogonal with each other. To verify the feasibility of the method, further simulations taking concomitant gradients into account, and using the Bloch equations, should be done. If the simulations are successful, it should be possible to add the GEE capability to the MEG-MRI prototype at Aalto University. At the moment, the main benefit of the GEE method is more theoretical; an addition to the selection of novel encoding possibilities offered by ULF MRI which are not feasible in conventional MRI.

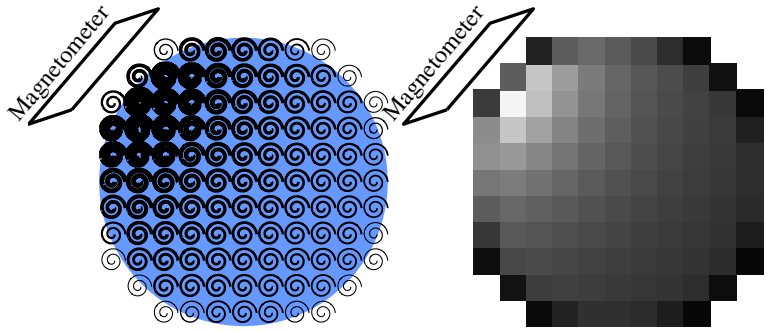

Figure 3.5. Illustration of the quantitaive ULF-MRI method. In the panel on the left, there is a sphere of water (in blue) where decaying precession of the nuclear spins (the spirals) is observed with a SQUID magnetometer. In this case, the strength of the observed signals, indicated with the spiral line thickness, depends on the water content of each voxel site and the position with respect to the magnetometer. The reconstructed image is presented in the right panel.

3.5 Publication V: "SQUID-sensor-based ultra-low-field MRI calibration with phantom images: Towards quantitative imaging"

In Publication V, the ULF-MRI sequence, measurement geometry, relaxation effects, signal dephasing in a gradient field, B_p and B_1 inhomogeneity and the Fourier PSF, see Section 2.2.1) were considered in a way which allowed the quantitative estimation of water-phantom voxel signals, leading to pixel grayscale values with less than 10% deviations from measurements. The underlying situation is presented in Fig. 3.5, with a rectangular SQUID magnetometer pickup loop. The method demonstrates that it is feasible to quantitatively assess the water content of a ULF-MRI sample, which could find applications in *e.g.* medical studies of tissues, along with quantitative imaging of porous media. Reciprocally, with known measurement geometry and physical properties (relaxation times, spin density and temperature) of the sample, the ULF-MRI system may be calibrated by modelling the measurement quantitatively.

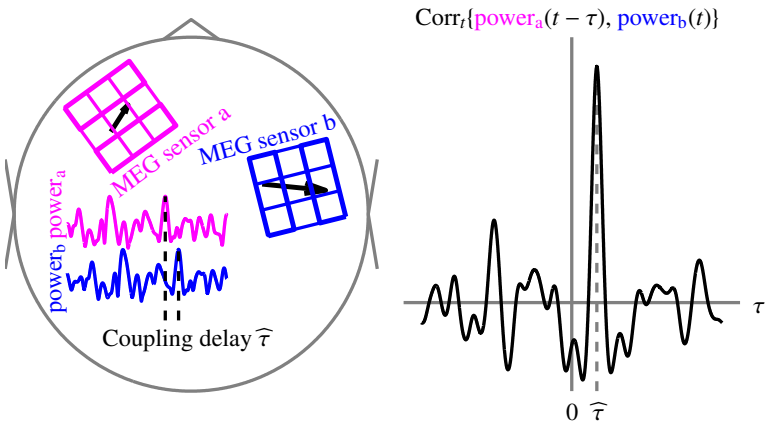

Figure 3.6. Illustration of the PC method. Left panel: In the head-top view with nose pointing up and ears on the sides, the PC coupling delay between brainwave ECDs (black arrows) a and b is $\widehat{\tau}$ (offset of $\mathrm{power_a}$ and $\mathrm{power_b}$). Right panel: Cross-correlation between the brainwave powers showing the coupling delay at delay $\tau = \widehat{\tau}$, where the cross-correlation is maximum.

3.6 Publication VI: "Detecting millisecond-range coupling delays between brainwaves in terms of power correlations by magnetoencephalography"

In Publication VI, a new method (power correlations, PCs) is presented for the determination of correlations and millisecond-range coupling delays between brainwaves at any two locations over the cortex (see Fig. 3.6). The method is based on using the power of signals measured with *e.g.* MEG or EEG. The method is first validated with a simulation study with a spherically symmetric head model with ECDs at selected locations with fixed tangential orientation and white noise that is partially correlated with different delays between two selected locations. The coupling delays were recovered with a few millisecond accuracy, depending on the SNR. Measurements with three subjects were also performed with durations of 10 to 30 min. The PC analysis revealed meaningful coupling delays in the millisecond range.

3.7 Results summary

The publications show that ULF MRI does not pose acute safety hazards if a magnetizable object is brought in the vicinity of the device (Publication I). The analysis methods for the FID signal make it easier to quantify the four parameters describing the FID, which can be used in simple NMR experiments with *e.g.* a ULF-MRI device (Publication II). It was shown that in LF MRI, it is feasible to use GMR mixed sensors to image samples at 1-mm^3 resolution (Publication III). For ULF MRI, the new method of GEE was proposed to accompany frequency and phase encodings (Publication IV). The possibility of quantitative ULF MRI was proposed and demonstrated, enabling the determination of water content of tissue and the calibration of the measurement system (Publication V). The method of power correlations (PCs) was proposed and applied on MEG measurements to yield coupling delays between brainwaves (Publication VI).

4. Discussion

The methods presented in this dissertation cover MRI from the conventional, ULF and LF points of view, accompanied by basic physics, signal processing and sensor technology. Although MRI is applicable to imaging any part of the body, brain imaging is of high value *i.a.* because of the high contrast that MRI can produce between brain tissues (especially grey and white matter) [ACR, 2013]. The contrast is based on the tissue-specific spin density ρ_s, and importantly the longitudinal (T_1) and transverse (T_2) relaxation times. However, when high contrast-to-noise ratio (CNR) is desired, it may be necessary to deliver intravenous contrast agents to the patient, especially in oncology (see *e.g.* [Strijkers et al., 2007]). It has been shown recently [Busch et al., 2012] that ULF MRI is also capable of detecting cancerous tissue. ULF MRI holds promise of high-CNR T_1-based imaging [Clarke et al., 2007]; an interesting characteristic is that biological tissues may have $T_1 \approx T_2$ at ultra-low fields [Vesanen et al., 2013b]. With the inherent insensitivity for susceptibility variations within tissue, ULF MRI may also produce images without any need for corrections of distortion. The demonstration of accurately quantitative ULF MRI (Publication V) may open new possibilites of determining ρ_s, T_1 and T_2 within the brain as well as the rest of the body, irrespective of susceptibility variations. Because the magnetic fields are orders of magnitude weaker than in conventional MRI and the geometry of the device is open, even most patients with medical implants or claustrophobia could be imaged; meticulous screening for magnetizable objects could be at least alleviated (Publication I).

When basic MR spectroscopy is performed, the most simple detectable signal is the FID which is characterised by four scalar parameters. In fact, it is possible to determine these parameters for several superimposed FIDs by the method of Prony analysis [Prony, 1795] which belongs to spectrum analysis [Kay and Marple, Jr, 1981]. The use of Prony analysis has become feasible with the help of computing [Hauer et al., 1990] and the Hankel total least-squares (TLS) method [Markovsky and Van Huffel, 2007]. Hankel TLS methods have been applied widely in MR spectroscopy

[Vanhamme et al., 2001, Laudadio et al., 2002, Poullet et al., 2008]. In the simpler case of a single FID, such as MR imaging a homogeneous sample without gradients, the four FID parameters can be determined in a simple fashion (Publication II).

In ULF MRI, the low magnetic fields add new simplicity to the design and operation of the necessary coils. It may be possible to utilize spatially varying prepolarization fields B_p to MR image encoding [Nieminen et al., 2010], or optimise the CNR [Nieminen et al., 2013] of some tissues. The adiabatic usage of the fields may open the possibility for CDI [Nieminen et al., 2014, Vesanen et al., 2014]. The mapping of sample temperature in ULF-MR images has also been demonstrated by experiment [Vesanen et al., 2013b]. To accompany the frequency and phase encoding methods, the new GEE method has been proposed (Publication IV). With this method, three-dimensional images with three different encoding methods, one in each orthogonal direction, would be possible. A limitation to this method may be posed by the concomitant gradients (see Section 2.5.2); this is left for future research.

LF MRI is perhaps closest to the MRI which was initially developed by R.V. Damadian, P.C. Lauterbur and P. Mansfield in the 1970s. Until the 1980s, the main field was generated by resistive coils, before the time of the superconducting MRI magnets [Larbalestier et al., 1986]. In LF MRI, while prepolarization can be used [Macovski and Conolly, 1993, Matter et al., 2006], images with good SNR and CNR can be obtained in a static field $B_0 \sim 10$ mT. This can be achieved with resistive coils, or GMR mixed sensors (Publication III). This is a dramatic demonstration of the field tolerance of the GMR mixed sensors which can recover from saturation after kilowatt-range RF pulses in a few microseconds [Pannetier-Lecoeur et al., 2010]. The applicability of GMR mixed sensors to biomagnetic measurements is still limited by the $1/f$-noise (of the order of 30 fT/Hz$^{1/2}$ at 10 Hz) which is large compared to SQUIDs (down to 1 fT/Hz$^{1/2}$ [Clarke et al., 2007]), but successful measurements in MCG have been performed [Pannetier-Lecoeur et al., 2011].

While GMR mixed sensors are currently not applicable, nor have atomic magnetometers yet made a breakthrough in MEG, SQUIDs continue to prevail. One of the challenges in solving the MEG inverse problem is the availability of an accurately co-registrable MRI image. While conventional MRI can be used for this, the subject must be physically moved from the MRI device to the MEG device. As the brain may reposition in the cerebospinal fluid (CSF) within the skull, mapping errors of a few millimetres could be expected. The moving from one device to the other is avoided in hybrid MEG-MRI, where the anatomy of the brain is imaged by the ULF MRI method and the function by MEG, all in one device (devices developed in the USA [Zotev et al., 2007a] and in Finland [Vesanen et al., 2013a] independent of each other). When the MEG-MRI technology matures, the mentioned mapping

errors can be suppressed and brain activity can be located with an unprecedented accuracy and precision; the possibility of simultaneous acquisition of biomagnetic and NMR signals has already been shown [Espy et al., 2005]. For example, the power couplings (PCs) between brainwaves measured by MEG and determined by a new method (Publication VI) could be mapped accurately between different parts of the cerebral cortex on the ULF MR images.

4.1 Conclusions

The methods developed in this dissertation work are related to ULF MRI, MEG and, in addition, LF MRI. The basic review on the underlying physics, signal processing and sensor technology in this dissertation gives the necessary foundation for understanding the methods. The description of conventional MRI helps in understanding LF MRI and ULF MRI. Most of the new methods were developed in connection with the EU project where a functional MEG-MRI device was designed and built. The most recent work enables detecting millisecond-range power couplings between brainwaves by MEG.

Errata

Publication III

Fig. 6, caption: "G_z- reading gradient" should be "G_x — reading gradient".

Bibliography

AA Abrikosov. On the magnetic properties of superconductors of the second group. *J Exp Theor Phys (USSR)*, 32:1441–1452, 1957.

ACR. ACR–ASNR–SPR practice guideline for the performance and interpretation of magnetic resonance imaging (MRI) of the brain, 2013. URL `http://www.acr.org/Quality-Safety/Standards-Guidelines/Practice-Guidelines-by-Modality/MRI`. Accessed 2014-01-30.

AI Ahonen, MS Hämäläinen, RJ Ilmoniemi, MJ Kajola, JET Knuutila, JT Simola, and VA Vilkman. Sampling theory for neuromagnetic detector arrays. *IEEE Trans Biomed Eng*, 40:859–869, 1993.

MN Baibich, JM Broto, A Fert, F Nguyen Van Dau, F Petroff, P Eitenne, G Creuzet, A Friedrich, and J Chazelas. Giant magnetoresistance of (001)Fe/(001)Cr magnetic superlattices. *Phys Rev Lett*, 61:2472–2475, 1988.

S Baillet, JC Mosher, and RM Leahy. Electromagnetic brain mapping. *IEEE Signal Process Mag*, 18:14–30, 2001.

J Bardeen, LN Cooper, and JR Schrieffer. Microscopic theory of superconductivity. *Phys Rev*, 106:162–164, 1957a.

J Bardeen, LN Cooper, and JR Schrieffer. Theory of superconductivity. *Phys Rev*, 108: 1175–1204, 1957b.

JW Belliveau, DN Kennedy, Jr, RC McKinstry, BR Buchbinder, RM Weisskoff, MS Cohen, JM Vevea, TJ Brady, and BR Rosen. Functional mapping of the human visual cortex by magnetic resonance imaging. *Science*, 254:716–719, 1991.

H Berger. Über das Elektrenkephalogramm des Menschen. *Archiv für Psychiatrie und Nervenkrankheiten*, 87:527–570, 1929.

M Blaimer, F Breuer, M Mueller, RM Heidemann, MA Griswold, and PM Jakob. SMASH, SENSE, PILS, GRAPPA. How to choose the optimal method. *Top Magn Reson Imaging*, 15:223–236, 2004.

N Bloembergen, EM Purcell, and RV Pound. Relaxation effects in nuclear magnetic resonance absorption. *Phys Rev*, 73:679–712, 1948.

D Brenner, J Lipton, L Kaufman, and SJ Williamson. Somatically evoked magnetic fields of the human brain. *Science*, 199:81–83, 1978.

M Burghoff, S Hartwig, and L Trahms. Nuclear magnetic resonance in the nanoTesla range. *Appl Phys Lett*, 87:054103, 2005.

M Burghoff, S Hartwig, W Kilian, A Vorwerk, and L Trahms. SQUID systems adapted to record nuclear magnetism in low magnetic fields. *IEEE Trans Appl Supercond*, 17:846–849, 2007.

M Burghoff, HH Albrecht, S Hartwig, I Hilschenz, R Körber, TS Thömmes, HJ Scheer, J Voigt, and L Trahms. SQUID system for MEG and low field magnetic resonance. *Metrol Meas Syst*, XVI:371–375, 2009.

S Busch, M Hatridge, M Mößle, W Myers, T Wong, M Mück, K Chew, K Kuchinsky, J Simko, and J Clarke. Measurements of T_1-relaxation in ex vivo prostate tissue at 132 μT. *Magn Reson Med*, 67:1138–1145, 2012.

G Buzsáki and A Draguhn. Neuronal oscillations in cortical networks. *Science*, 304:1926–1929, 2004.

HY Carr and EM Purcell. Effects of diffusion on free precession in nuclear magnetic resonance experiments. *Phys Rev*, 94:630–638, 1954.

D-X Chen, JA Burg, and RB Goldfarb. Demagnetizing factors for cylinders. *IEEE Trans Magn*, 27:3601–3619, 1991.

M Chukharkin, A Kalabukhov, JF Schneiderman, F Öisjöen, M Jönsson, M Xie, OV Snigirev, and D Winkler. Improvement of ultra-low field magnetic resonance recordings with a multilayer flux-transformer-based high-T_c SQUID magnetometer. *IEEE Trans Appl Supercond*, 23:6384681, 2013.

J Clarke and AI Braginski, editors. *The SQUID Handbook: Vol. I Fundamentals and Technology of SQUIDs and SQUID Systems*. Wiley-VCH, Weinheim, Germany, 2004.

J Clarke, M Hatridge, and M Mößle. SQUID-detected magnetic resonance imaging in microtesla fields. *Annu Rev Biomed Eng*, 9:389–413, 2007.

D Cohen. Magnetoencephalography: Evidence of magnetic fields produced by alpha-rhythm currents. *Science*, 161:784–786, 1968.

D Cohen. Large-volume conventional magnetic shields. *Rev Phys Appl*, 5:53–58, 1970.

D Cohen. Magnetoencephalography: Detection of the brain's electrical activity with a superconducting magnetometer. *Science*, 175:664–666, 1972.

D Cohen, U Schläpfer, S Ahlfors, M Hämäläinen, and E Halgren. New six-layer magnetically-shielded room for MEG. In H Nowak, J Haueisen, F Gießler, and R Huonker, editors, *Proceedings BIOMAG 2002. 13th International Conference on Biomagnetism*, pages 919–921, 2002.

LN Cooper. Bound electron pairs in a degenerate Fermi gas. *Phys Rev*, 104:1189–1190, 1956.

RV Damadian. Apparatus and method for detecting cancer in tissue. US Patent 3789832, 1972.

HB Dang, AC Maloof, and MV Romalis. Ultrahigh sensitivity magnetic field and magnetization measurements with an atomic magnetometer. *Appl Phys Lett*, 97:151110, 2010.

F Darvas, D Pantazis, E Kucukaltun-Yildirim, and RM Leahy. Mapping human brain function with MEG and EEG: methods and validation. *NeuroImage*, 23:S289–S299, 2004.

BS Deaver, Jr and WM Fairbank. Experimental evidence for quantized flux in superconducting cylinders. *Phys Rev Lett*, 7:43–46, 1961.

R Doll and M Näbauer. Experimental proof of magnetic flux quanitzation in a superconducting ring. *Phys Rev Lett*, 7:51–52, 1961.

DL Donoho. Compressed sensing. *IEEE Trans Inform Theory*, 52:1289–1306, 2006.

H Dyvorne, C Fermon, M Pannetier-Lecoeur, H Polovy, and A-L Walliang. NMR with superconducting-GMR mixed sensors. *IEEE Trans Appl Supercond*, 19:819–822, 2009.

M Espy, A Matlashov, and P Volegov. SQUID-detected ultra-low field MRI. *J Magn Reson*, 228:1–15, 2013.

MA Espy, AN Matlachov, PL Volegov, JC Mosher, and RH Kraus, Jr. SQUID-based simultaneous detection of NMR and biomagnetic signals at ultra-low magnetic fields. *IEEE Trans Appl Supercond*, 15:635–639, 2005.

JH Friedman and JW Tukey. A projection pursuit algorithm for exploratory data analysis. *IEEE Trans Comput*, c-23:881–890, 1974.

NG Gençer and SJ Williamson. Differential characterization of neural sources with the bimodal truncated SVD pseudo-inverse for EEG and MEG measurements. *IEEE Trans Biomed Eng*, 45:827–838, 1998.

VL Ginzburg. On superconductivity and superfluidity (What I have and have not managed to do), as well as on the 'physical minimum' at the beginning of the 21st century. *Chem Phys Chem*, 5:930–945, 2004.

VL Ginzburg and LD Landau. On the theory of superconductivity. *Žu Eksper Teor Fiz*, 20: 1064, 1950.

LP Gor'Kov. Microscopic derivation of the Ginzburg-Landau equations in the theory of superconductivity. *Sov Phys JETP*, 9:1364, 1959.

V Gras, Z Abbas, and NJ Shah. Spoiled FLASH MRI with slice selective excitation: Signal equation with a correction term. *Concepts Magn Reson Part A*, 42:89–100, 2013.

R Grech, T Cassar, J Muscat, KP Camilleri, SG Fabri, M Zervakis, P Xanthopoulos, V Sakkalis, and B Vanrumste. Review on solving the inverse problem in EEG source analysis. *J Neuroeng Rehabil*, 5:25, 2008.

YS Greenberg. Application of superconducting quantum interference devices to nuclear magnetic resonance. *Rev Mod Phys*, 70:175–222, 1998.

MA Griswold, PM Jakob, M Nittka, JW Goldfarb, and A Haase. Partially parallel imaging with localized sensitivities (PILS). *Magn Reson Med*, 44:602–609, 2000.

MA Griswold, PM Jakob, RM Heidemann, M Nittka, V Jellus, J Wang, B Kiefer, and A Haase. Generalized autocalibrating partially parallel acquisitions (GRAPPA). *Magn Reson Med*, 47:1202–1210, 2002.

F Grynszpan and DB Geselowitz. Model studies of the magnetocardiogram. *Biophys J*, 13: 911–925, 1973.

EL Hahn. Spin echoes. *Phys Rev*, 80:580–594, 1950.

M Hämäläinen, R Hari, RJ Ilmoniemi, J Knuutila, and OV Lounasmaa. Magnetoencephalography—theory, instrumentation, and applications to noninvasive studies of the working human brain. *Rev Mod Phys*, 65:413–497, 1993.

MS Hämäläinen and RJ Ilmoniemi. Interpreting magnetic fields of the brain: minimum norm estimates. *Med Biol Eng Comp*, 32:35–42, 1994.

R Hari and R Salmelin. Human cortical oscillations: a neuromagnetic view through the skull. *Trends Neurosci*, 20:44–49, 1997.

R Hari and R Salmelin. Magnetoencephalography: From SQUIDs to neuroscience. Neuroimage 20th anniversary special edition. *NeuroImage*, 61:386–396, 2012.

JF Hauer, CJ Demeure, and LL Scharf. Initial results in Prony analysis of power system response signals. *IEEE Trans Power Syst*, 5:80–89, 1990.

I Hilschenz, R Körber, HJ Scheer, T Fedele, HH Albrecht, A Mario Cassará, S Hartwig, L Trahms, J Haase, and M Burghoff. Magnetic resonance imaging at frequencies below 1 kHz. *Magn Reson Imaging*, 31:171–177, 2013.

JF Hipp, DJ Hawellek, M Corbetta, M Siegel, and AK Engel. Large-scale cortical correlation structure of spontaneous oscillatory activity. *Nature Neurosci*, 15:884–890, 2012.

Y-C Hsu, PT Vesanen, JO Nieminen, KCJ Zevenhoven, J Dabek, L Parkkonen, I-L Chern, RJ Ilmoniemi, and F-H Lin. Efficient concomitant and remanence field artifact reduction in ultra-low-field MRI using a frequency-space formulation. *Magn Reson Med*, In press: 1–11, 2013.

A Hyvärinen, J Karhunen, and E Oja. *Independent Component Analysis*. John Wiley & Sons, New York, 2001.

A Hyvärinen, P Ramkumar, L Parkkonen, and R Hari. Independent component analysis of short-term Fourier transforms for spontaneous EEG/MEG analysis. *NeuroImage*, 49: 257–271, 2010.

B Inglis, K Buckenmaier, P SanGiorgio, AF Pedersen, MA Nichols, and J Clarke. MRI of the human brain at 130 microtesla. *Proc Natl Acad Sci*, 110:19194–19201, 2013.

JD Jackson. *Classical Electrodynamics*. Wiley, USA, 1999.

D Jiles. *Magnetism and Magnetic Materials*. CRC Press, Boca Raton, Florida, 1998.

SR Jones, DL Pritchett, MA Sikora, SM Stufflebeam, M Hämäläinen, and CI Moore. Quantitative analysis and biophysically realistic neural modeling of the MEG mu rhythm: Rhythmogenesis and modulation of sensory-evoked responses. *J Neurophysiol*, 102:3554–3572, 2009.

BD Josephson. Possible new effects in superconductive tunneling. *Phys Lett*, 1:251–253, 1962.

BD Josephson. The discovery of tunneling supercurrents. *Rev Mod Phys*, 46:251–254, 1974.

SM Kay and SL Marple, Jr. Spectrum analysis—a modern perspective. *Proc IEEE*, 69: 1380–1419, 1981.

K Kim, S Begus, H Xia, S-K Lee, V Jazbinsek, Z Trontelj, and MV Romalis. Multi-channel atomic magnetometer for magnetoencephalography: A configuration study. *NeuroImage*, 89:143–151, 2014.

S Knappe-Grueneberg, A Schnabel, G Wuebbeler, and M Burghoff. Influence of demagnetization coil configuration on residual field in an extremely magnetically shielded room: Model and measurements. *J Appl Phys*, 103:07E925, 2008.

R Körber, JO Nieminen, N Höfner, V Jazbinšek, H-J Scheer, K Kim, and M Burghoff. An advanced phantom study assessing the feasibility of neural current imaging by ultra-low-field NMR. *J Magn Reson*, 237:182–190, 2013.

RH Kraus, Jr, P Volegov, A Matlachov, and M Espy. Toward direct neural current imaging by resonant mechanisms at ultra-low field. *NeuroImage*, 39:310–317, 2008.

D Larbalestier, G Fisk, B Montgomery, and D Hawksworth. High-field superconductivity. Rapid strides in the development of composite superconducting materials have encouraged the widespread use of high-field superconducting magnets in high-energy physics, fusion and medical imaging—fulfilling Kamerlingh Onnes's 75-year-old vision. *Phys Today*, 39 (3):24–33, 1986.

T Laudadio, M Mastronardi, L Vanhamme, P Van Hecke, and S Van Huffel. Improved Lanczos algorithms for blackbox MRS data quantitation. *J Magn Reson*, 157:292–297, 2002.

M Le Van Quyen and A Bragin. Analysis of dynamic brain oscillations: methodological advances. *Trends Neurosci*, 30:365–373, 2007.

JE Lenz. A review of magnetic sensors. *Proc IEEE*, 78:973–989, 1990.

Z-P Liang and PC Lauterbur. *Principles of Magnetic Resonance Imaging: A Signal Processing Perspective*. IEEE Press, New York, USA, 2000.

F London. On the problem of the molecular theory of superconductivity. *Phys Rev*, 74: 562–573, 1948.

F London and H London. The electromagnetic equations of the superconductor. *Proc R Soc Lond*, 149:71–88, 1935.

J Luomahaara, PT Vesanen, J Penttilä, JO Nieminen, J Dabek, J Simola, M Kiviranta, L Grönberg, CJ Zevenhoven, RJ Ilmoniemi, and J Hassel. All-planar SQUIDs and pickup coils for combined MEG and MRI. *Supercond Sci Technol*, 24:075020, 2011.

M Lustig, D Donoho, and JM Pauly. Sparse MRI: The application of compressed sensing for rapid MR imaging. *Magn Reson Med*, 58:1182–1195, 2007.

A Macovski and S Conolly. Novel approaches to low-cost MRI. *Magn Reson Med*, 30: 221–230, 1993.

AJ Mager. Magnetic shields. *IEEE Trans Magn*, MAG-6:67–75, 1970.

PE Magnelind, JJ Gomez, AN Matlashov, T Owens, JH Sandin, PL Volegov, and MA Espy. Co-registration of interleaved MEG and ULF MRI using a 7 channel low-T_c SQUID system. *IEEE Trans Appl Supercond*, 21:456–460, 2011.

P Mansfield. Multi-planar image formation using NMR spin echoes. *J Phys C Solid State Phys*, 10:L55–L58, 1977.

I Markovsky and S Van Huffel. Overview of total least-squares methods. *Sign Proc*, 87: 2283–2302, 2007.

AN Matlashov, E Burmistrov, PE Magnelind, L Schultz, AV Urbaitis, PL Volegov, J Yoder, and MA Espy. SQUID-based systems for co-registration of ultra-low field nuclear magnetic images and magnetoencephalography. *Physica C*, 482:19–26, 2012.

NI Matter, GC Scott, T Grafendorfer, A Macovski, and SM Conolly. Rapid polarizing field cycling in magnetic resonance imaging. *IEEE Trans Med Imaging*, 25:84–93, 2006.

R McDermott, AH Trabesinger, M Mück, EL Hahn, A Pines, and J Clarke. Liquid-state NMR and scalar couplings in microtesla magnetic fields. *Science*, 295:2247–2249, 2002.

R McDermott, SK Lee, B ten Haken, AH Trabesinger, A Pines, and J Clarke. Microtesla MRI with a superconducting quantum interference device. *Proc Natl Acad Sci*, 101:7857–7861, 2004.

JC Mosher, PS Lewis, and RM Leahy. Multiple dipole modeling and localization from spatio-temporal MEG data. *IEEE Trans Biomed Eng*, 39:541–557, 1992.

JC Mosher, RM Leahy, and PS Lewis. EEG and MEG : Forward solutions for inverse methods. *IEEE Trans Biomed Eng*, 46:245–259, 1999.

M Mößle, WR Myers, S-K Lee, N Kelso, M Hatridge, A Pines, and J Clarke. SQUID-detected in vivo MRI at microtesla magnetic fields. *IEEE Trans Appl Supercond*, 15: 757–760, 2005.

S Murakami and Y Okada. Contributions of principal neocortical neurons to magnetoencephalography and electroencephalography signals. *J Physiol*, 575.3:925–936, 2006.

W Myers, D Slichter, M Hatridge, S Busch, M Mößle, R McDermott, AS Trabesinger, and J Clarke. Calculated signal-to-noise ratio of MRI detected with SQUIDs and Faraday detectors in fields from 10 μT to 1.5 T. *J Magn Reson*, 186:182–192, 2007.

WR Myers, M Mößle, and J Clarke. Correction of concomitant gradient artifacts in experimental microtesla MRI. *J Magn Reson*, 177:274–284, 2005.

R Näätänen. The perception of speech sounds by the human brain as reflected by the mismatch negativity (MMN) and its magnetic equivalent (MMNm). *Psychophysiology*, 38: 1–21, 2001.

E Niedermeyer and F Lopes da Silva. *Electroencephalography. Basic Principles, Clinical Applications, and Related Fields*. Lippincott Williams & Wilkins, Philadelphia, Pennsylvania, 2005.

JO Nieminen and RJ Ilmoniemi. Solving the problem of concomitant gradients in ultra-low-field MRI. *J Magn Reson*, 207:213–219, 2010.

JO Nieminen, M Burghoff, L Trahms, and RJ Ilmoniemi. Polarization encoding as a novel approach to MRI. *J Magn Reson*, 202:2011–2016, 2010.

JO Nieminen, PT Vesanen, KCJ Zevenhoven, J Dabek, J Hassel, J Luomahaara, JS Penttilä, and RJ Ilmoniemi. Avoiding eddy-current problems in ultra-low-field MRI with self-shielded polarizing coils. *J Magn Reson*, 212:154–160, 2011.

JO Nieminen, J Voigt, S Hartwig, HJ Scheer, M Burghoff, L Trahms, and RJ Ilmoniemi. Improved contrast in ultra-low-field MRI with time-dependent bipolar prepolarizing fields: Theory and NMR demonstrations. *Metrol Meas Syst*, 20:327–336, 2013.

JO Nieminen, KC Zevenhoven, PT Vesanen, YC Hsu, and RJ Ilmoniemi. Current-density imaging using ultra-low-field MRI with adiabatic pulses. *Magn Reson Imaging*, 32:54–59, 2014.

VV Nikulin, G Nolte, and G Curio. A novel method for reliable and fast extraction of neuronal EEG/MEG oscillations on the basis of spatio-spectral decomposition. *NeuroImage*, 55:1528–1535, 2011.

H Nyquist. Thermal agitation of electric charge in conductors. *Phys Rev*, 32:110–113, 1928.

OECD. Organisation for Economic Co-operation and Development (OECD), 2013. URL `http://www.oecd.org/statistics`. Accessed 2014-01-30.

S Ogawa, DW Tank, R Menon, JM Ellermann, S-G Kim, H Merkle, and K Ugurbil. Intrinsic signal changes accompanying sensory stimulation: Functional brain mapping with magnetic resonance imaging. *Proc Natl Acad Sci*, 89:5951–5955, 1992.

F Öisjöen, JF Schneiderman, GA Figueras, ML Chukharkin, A Kalabukhov, A Hedström, M Elam, and D Winkler. High-T_c superconducting quantum interference device recordings of spontaneous brain activity: Towards high-T_c magnetoencephalography. *Appl Phys Lett*, 100:132601, 2012.

HK Onnes. Investigations into the properties of substances at low temperatures, which have led, amongst other things, to the preparation of liquid helium. In S Lundqvist, editor, *Nobel Lectures in Physics*, pages 306–336. World Scientific, Singapore, 1998.

ACE Onslow, R Bogacz, and MW Jones. Quantifying phase–amplitude coupling in neuronal network oscillations. *Prog Biophys Mol Biol*, 105:49–57, 2011.

JA Osborn. Demagnetizing factors of the general ellipsoid. *Phys Rev*, 67:351–357, 1945.

D Oyama, Y Adachi, N Hatsusaka, T Kasahara, M Yumoto, I Hashimoto, and G Uehara. Evaluation of an isosceles-triangle-coil phantom for magnetoencephalography. *IEEE Trans Magn*, 47:3853–3856, 2011.

S Palva and JM Palva. Discovering oscillatory interaction networks with M/EEG: challenges and breakthroughs. *Trends Cogn Sci*, 16:219–230, 2012.

M Pannetier, C Fermon, G Le Goff, J Simola, and E Kerr. Femtotesla magnetic field measurement with magnetoresistive sensors. *Science*, 304:1648–1650, 2004.

M Pannetier, C Fermon, G Legoff, J Simola, E Kerr, M Welling, and RJ Wijngaarden. Ultrasensitive field sensors—An alternative to SQUIDs. *IEEE Trans Appl Supercond*, 15:892–895, 2005.

M Pannetier-Lecoeur, C Fermon, H Dyvorne, JF Jacquinot, H Polovy, and AL Walliang. Magnetoresistive-superconducting mixed sensors for biomagnetic applications. *J Magn Magn Mater*, 322:1647–1650, 2010.

M Pannetier-Lecoeur, L Parkkonen, N Sergeeva-Chollet, H Polovy, C Fermon, and C Fowley. Magnetocardiography with sensors based on giant magnetoresistance. *Appl Phys Lett*, 98: 153705, 2011.

LT Parkkonen, JT Simola, JT Tuoriniemi, and AI Ahonen. An interference suppression system for multichannel magnetic field detector arrays. In T Yoshimoto, M Kotani, S Kuriki, H Karibe, and N Nakasato, editors, *Recent Advances in Biomagnetism, Sendai, Japan*, pages 13–16, 1999.

A Pasquarelli, M De Melis, L Marzetti, H-P Müller, and SN Erné. Calibration of a vector-MEG helmet system. *Neurol Clin Neurophysiol*, 94:1–4, 2004.

K Pearson. On lines and planes of closest fit to systems of points in space. *Philosoph Magaz*, 2:559–572, 1901.

J-B Poullet, DM Sima, and S Van Huffel. MRS signal quantitation: A review of time- and frequency-domain methods. *J Magn Reson*, 195:134–144, 2008.

R Prony. Essay expérimental et analytique. Sur les lois de la dilatabilité des fluides élastiques et sur celles de la force expansive de la vapeur de l'eau et de la vapeur de l'alkool à différentes températures. *Journal de l'École Polytechnique floréal et Plairial, an III*, 1: 24–76, 1795.

KP Pruessmann, M Weiger, MB Scheidegger, and P Boesiger. SENSE: Sensitivity encoding for fast MRI. *Magn Reson Med*, 42:952–962, 1999.

R Reyment and KG Jöreskog. *Applied Factor Analysis in the Natural Sciences*. Cambridge University Press, Cambridge, 1996.

P Ripka. Advances in fluxgate sensors. *Sens Actuators A*, 106:8–14, 2003.

PB Roemer, WA Edelstein, CE Hayes, SP Souza, and OM Mueller. The NMR phased array. *Magn Reson Med*, 16:192–225, 1990.

J Ruiz-Cabello, BP Barnett, PA Bottomley, and JWM Bulte. Fluorine (^{19}F) MRS and MRI in biomedicine. *NMR Biomed*, 24:114–129, 2011.

J Sarvas. Basic mathematical and electromagnetic concepts of the biomagnetic inverse problem. *Phys Med Biol*, 32:11–22, 1987.

IM Savukov, VS Zotev, PL Volegov, MA Espy, AN Matlashov, JJ Gomez, and RH Kraus Jr. MRI with an atomic magnetometer suitable for practical imaging applications. *J Magn Reson*, 199:188–191, 2009.

R Sepponen. Apparatus and method for the examination of properties of an object. US Patent 4906931, Instrumentarium Corp., Finland, 1990.

W Shao, G Wang, R Fuzesy, EW Hughes, BA Chronik, GC Scott, SM Conolly, and A Macovski. Low readout field magnetic resonance imaging of hyperpolarized xenon and water in a single system. *Appl Phys Lett*, 80:2032–2034, 2002.

AH Silver and JE Zimmerman. Quantum transitions and loss in multiply connected superconductors. *Phys Rev Lett*, 15:888–891, 1965.

R Sinibaldi, C De Luca, JO Nieminen, A Galante, V Pizzella, P Sebastiani, M Pannetier-Lecoeur, A Manna, P Chiacchiaretta, G Tamburro, A Sotgiu, C Fermon, GL Romani, and S Della Penna. NMR detection at 8.9 mT with a GMR based sensor coupled to a superconducting Nb flux transformer. *Prog Electromagn Research*, 142:389–408, 2013.

NB Smith and A Webb. *Introduction to Medical Imaging. Physics, Engineering and Clinical Applications*. Cambridge University Press, Cambridge, 2011.

DK Sodickson and WJ Manning. Simultaneous acquisition of spatial harmonics (SMASH): Fast imaging with radiofrequency coil arrays. *Magn Reson Med*, 38:591–603, 1997.

J Stepišnik, V Eržen, and M Kos. NMR imaging in the earth's magnetic field. *Magn Reson Med*, 15:386–391, 1990.

GJ Strijkers, WJM Mulder, GAF van Tilborg, and K Nicolay. MRI contrast agents: Current status and future perspectives. *Anticancer Agents Med Chem*, 7:291–305, 2007.

BH Suits, AN Garroway, and JB Miller. Surface and gradiometer coils near a conducting body: The lift-off effect. *J Magn Reson*, 135:373–379, 1998.

S Taulu, M Kajola, and J Simola. Suppression of interference and artifacts by the signal space separation method. *Brain Topogr*, 16:269–275, 2004.

ABL Tort, R Komorowski, H Eichenbaum, and N Kopell. Measuring phase-amplitude coupling between neuronal oscillations of different frequencies. *J Neurophysiol*, 104:1195–1210, 2010.

MA Uusitalo and RJ Ilmoniemi. Signal-space projection method for separating MEG or EEG into components. *Med Biol Eng Comput*, 35:135–140, 1997.

D van Delft and P Kes. The discovery of superconductivity. *Phys Today*, 63:38–43, 2010.

BD Van Veen, W van Drongelen, M Yuchtman, and A Suzuki. Localization of brain electrical activity via linearly constrained minimum variance spatial filtering. *IEEE Trans Biomed Eng*, 44:867–880, 1997.

L Vanhamme, T Sundin, P Van Hecke, and S Van Huffel. MR spectroscopy quantitation: a review of time-domain methods. *NMR Biomed*, 14:233–246, 2001.

PT Vesanen, JO Nieminen, KCJ Zevenhoven, J Dabek, J Simola, J Sarvas, and RJ Ilmoniemi. The spatial and temporal distortion of magnetic fields applied inside a magnetically shielded room. *IEEE Trans Magn*, 48:53–61, 2012.

PT Vesanen, JO Nieminen, KCJ Zevenhoven, J Dabek, LT Parkkonen, AV Zhdanov, J Luomahaara, J Hassel, J Penttilä, J Simola, AI Ahonen, JP Mäkelä, and RJ Ilmoniemi. Hybrid ultra-low-field MRI and magnetoencephalography system based on a commercial whole-head neuromagnetometer. *Magn Reson Med*, 69:1795–1804, 2013a.

PT Vesanen, KCJ Zevenhoven, JO Nieminen, J Dabek, LT Parkkonen, and RJ Ilmoniemi. Temperature dependence of relaxation times and temperature mapping in ultra-low-field MRI. *J Magn Reson*, 235:50–57, 2013b.

PT Vesanen, JO Nieminen, KCJ Zevenhoven, Y-C Hsu, and RJ Ilmoniemi. Current-density imaging using ultra-low-field MRI with zero-field encoding. *Magn Reson Imaging*, Accepted for publication (doi: 10.1016/j.mri.2014.01.012), 2014.

PL Volegov, JC Mosher, MA Espy, and RH Kraus, Jr. On concomitant gradients in low-field MRI. *J Magn Reson*, 175:103–113, 2005.

K Zevenhoven. Solving transient problems in ultra-low-field MRI. MSc Thesis, Aalto University School of Science, Helsinki, Finland, 2011.

K Zevenhoven and RJ Ilmoniemi. Performance of SQUID sensor arrays for MRI of the brain. In *Proceedings of the 19th Annual Meeting of ISMRM, Montreal, Canada*, page 4226, 2011.

KCJ Zevenhoven and S Alanko. Ultra-low-noise amplifier for ultra-low-field MRI main field and gradients. *Accepted for publication*, 2014.

KCJ Zevenhoven, S Busch, M Hatridge, F Öisjöen, RJ Ilmoniemi, and J Clarke. Conductive shield for ultra-low-field magnetic resonance imaging: theory and measurements of eddy currents. *J Appl Phys (in review)*, 2014.

VS Zotev, AN Matlashov, PL Volegov, HJ Sandin, MA Espy, JC Mosher, AV Urbaitis, SG Newman, and RH Kraus Jr. Multi-channel SQUID system for MEG and ultra-low-field MRI. *IEEE Trans Appl Supercond*, 17:839–842, 2007a.

VS Zotev, AN Matlashov, PL Volegov, AV Urbaitis, MA Espy, and RH Kraus Jr. SQUID-based instrumentation for ultralow-field MRI. *Supercond Sci Tech*, 20:S367–S373, 2007b.

VS Zotev, PL Volegov, AN Matlashov, MA Espy, JC Mosher, and RH Kraus Jr. Parallel MRI at microtesla fields. *J Magn Reson*, 192:197–208, 2008.

VS Zotev, T Owens, AN Matlashov, IM Savukov, JJ Gomez, and MA Espy. Microtesla MRI with dynamic nuclear polarization. *J Magn Reson*, 207:78–88, 2010.

Non-invasive and safe brain imaging methods are very important medically and for understanding human behaviour. During recent decades, these imaging methods have been developed substantially, with certain further improvements suggested in this thesis work. In medicine, especially diagnostic applications are important for the planning of treatment. In research, imaging methods can be applied in controlled but naturalistic conditions to yield new information on brain function.

In this thesis work, new methods for ultra-low-field and low-field magnetic resonance imaging (MRI), magnetoencephalography (MEG) and their combination were developed. MRI shows the structure of the brain with unique contrast and with MEG the subtle magnetic fields generated by the weak cortical electric currents can be measured, describing cortical activation. The methods developed in this thesis work enhance, for example, the determination of tissue water content and couplings between brain areas.

Aalto-DD 42/2014

ISBN 978-952-60-5629-6
ISBN 978-952-60-5630-2 (pdf)
ISSN-L 1799-4934
ISSN 1799-4934
ISSN 1799-4942 (pdf)

Aalto University
School of Science
Dept. of Biomedical Engineering and Computational Science
www.aalto.fi

BUSINESS + ECONOMY

ART + DESIGN + ARCHITECTURE

SCIENCE + TECHNOLOGY

CROSSOVER

DOCTORAL DISSERTATIONS